Instrument Artifacts Lead to Uncertainties in Parameterizations of Cloud Condensation Nucleation

Jessica A. Mirrielees and Sarah D. Brooks

Texas A&M University, College Station, TX 77843

Correspondence E-mail: jmirrielees@tamu.edu

Abstract

The concentrations of cloud condensation nuclei (CCN) modulate cloud properties, rainfall location and intensity, and climate forcings. This work assesses uncertainties in CCN measurements and the apparent hygroscopicity parameter (κ_{app}) which is widely used to represent CCN populations in climate models. CCN measurements require accurate operation of three instruments: the CCN instrument, the differential mobility analyzer (DMA), and the condensation particle counter (CPC). Assessment of DMA operation showed that varying the ratio of aerosol to sheath flow from 0.05 to 0.30 resulted in discrepancies between the κ_{app} values calculated from CCN measurements and the literature value. Discrepancies were found to increase from effectively zero to 0.18 for sodium chloride, and from effectively zero to 0.08 for ammonium sulfate. The ratio of excess to sheath flow was also varied, which shifted the downstream aerosol distribution towards smaller particle diameters (for excess flow < sheath flow) or larger particle diameters (for excess flow > sheath flow) than predicted. For the CPC instrument, undercounting occurred at high concentrations, resulting in calculated κ_{app} lower than the literature values. Lastly, undercounting by CCN instruments at high concentration was also assessed, taking the effect of supersaturation on counting efficiency into account. Under recommended operating conditions, the combined DMA, CPC, and CCN uncertainties in κ_{app} are 1.1 % or less for 25 to 200 nm diameter aerosols.

Copyright Statement

Will be provided by Copernicus.

1. Introduction

Aerosol-cloud interactions represent a major uncertainty in current predictions of the Earth's climate (IPCC, 2013). According to well-known Köhler theory, an aerosol's potential to catalyze cloud droplet formation by activating as a cloud condensation nucleus (CCN) depends on its physical and chemical properties. For any given composition, the CCN activation potential of an aerosol increases as its diameter decreases. While the relationship between aerosol diameter and CCN activation is straightforward, the effect of composition on an aerosol's ability to participate in cloud formation is more complex (Petters and Kreidenweis, 2013; Ovadnevaite et al., 2011). Predicting the cloud forming capacity of various air masses based on the properties of the aerosol they contain is essential for evaluating relative contributions from pollution, continental background and marine aerosol sources (Brooks and Thornton, 2018; Carslaw et al., 2013). Long-term CCN measurements are available from numerous locations globally (Schmale et al., 2018). However, understanding regional and temporal variability in CCN populations requires the ability to assess whether observed differences reflect true physical differences or simply variations in CCN sampling strategies.

Parameterizations of CCN activity which accurately prescribe CCN measurements are needed for climate models, cloud resolving models, and air quality predictions (Betancourt and Nenes, 2014; Betancourt et al., 2013; Chang et al., 2017; Crosbie et al., 2015; Karydis et al., 2012; Kawecki and Steiner, 2018). One parameterization was designed to represent the cloud droplet activation potential ambient aerosol masses of unknown composition with a single variable, kappa (κ) based on the dry aerosol's hygroscopicity, or ability to uptake water and form a solution droplet (Petters and Kreidenweis, 2007). Various names and abbreviations have been given to κ throughout the literature: "hygroscopicity parameter", "single hygroscopicity parameter", κ (Petters and Kreidenweis, 2007;

Carrico et al., 2008; Asa-Awuku et al., 2010; Moore et al., 2012b); "CCN-derived κ", κ_{CCN} (Carrico et al., 2008; Petters and Kreidenweis, 2007); and the "apparent hygroscopicity parameter" κ_{app} (Sullivan et al., 2009; Collins et al., 2016; Petters and Kreidenweis, 2013). The term *apparent* hygroscopicity is favored by many because it emphasizes that fact that while CCN activation can often be predicted accurately by hygroscopic water uptake, they are different physical processes. It is possible for a compound to have high intrinsic hygroscopicity and low apparent hygroscopicity if it is poorly soluble in water (Sullivan et al., 2009).

Parameterizations of hygroscopicity that pre-date Petters and Kreidenweiss 2007 exist as well. Winkler 1973 developed an equation for approximating the growth of an aerosol particle with relative humidity, based on the quantity and physical characteristics of the soluble species in the particle. Another approximation for the relationship between the equilibrium size of a particle and relative humidity was derived by Fitzgerald in 1975, in which the soluble fraction and composition of the soluble component(s) are taken into account.

Fitzgerald et al., 1982 derived a particle composition parameter using the mass fraction and physical properties of soluble material in a particle. Kreidenweis et al., 2005 determined that the critical activation diameter of dry aerosol particles can be calculated from simplified Köhler theory using the physical properties of water and the solute in a solution droplet. This parameterization has been used in CCN closure studies (Bougiatioti et al., 2009; Moore et al., 2011; Moore et al., 2012a). The earliest prediction of CCN concentrations for specific particle diameters and hygroscopicity used this parameterization as well (Mochida et al., 2006).

Once calculated, hygroscopicity parameters are useful tools for comparing CCN field measurements conducted in various regions and seasons and for making predictions about cloud formation, aerosol-cloud interactions in weather, and climate models. Values of κ_{app} can be used to compare the CCN results in field and laboratory studies, including sea spray aerosol. For example, aggregation of results from several mesocosm experiments and marine field studies found submicron (30-100 nm) κ_{app} for sea spray aerosol as low as 0.4 and as high 1.3 (Collins et al., 2016). Another study, which included a survey of observational CCN data, reported that marine and continental aerosols could be described by κ_{app} values of 0.7 ± 0.2 and 0.3 ± 0.1 respectively (Andreae and Rosenfeld, 2008).

Several studies have examined the sensitivity of models to κ values derived from HTDMA measurements. An analysis of the NASA Global Modeling Initiative Chemical Transport Model and the GEOS-Chem CTM (Karydis et al., 2012) found that cloud droplet number concentration is sensitive to κ in Arctic and remote regions, where background aerosol loadings are low. Another study (Betancourt and Nenes, 2014) found that a ±50 % uncertainty range in the κ of secondary organic aerosols and particulate organic matter resulted in a cloud droplet number concentration uncertainty of up to 15 % and 16 %, respectively. Updating precipitation models with lab-derived κ values for specific inorganic and organic species may increase the accuracy of storm forecasts by providing better predictions of intense precipitation (Kawecki and Steiner, 2018). In terms of climate, (Liu and Wang, 2010) found that increasing the κ of primary organic aerosols from 0 to 0.1, and decreasing the κ of secondary organics aerosols from 0.14 to 0.07, resulted in an uncertainty in global secondary aerosol indirect forcing of 0.4 Wm^{-2} from pre-industrial times to present day.

The sensitivity of weather and climate models to hygroscopicity parameters demonstrates the need for accurate measurements. In this study, we examine experimental uncertainties in CCN measurements and

the resulting uncertainties in determination of κ_{app}. Differences in report κ_{app} values may result from experimental artifacts rather any actual differences in aerosol's ability to facilitate cloud formation. By systematically quantifying sources of experimental error, this study provides a framework for determining the significance of variations in CCN properties reported in multiple studies and defining the operating conditions which minimize instrumental artifacts.

2. Background

The Köhler equation relates water vapor saturation ratio at the surface of a wet droplet, s, to its radius at equilibrium (Rogers and Yau, 1989):

$$s = \left(1 - \frac{b}{r^3}\right) \exp\left(\frac{a}{r}\right) \quad (1a)$$

$$a = \frac{2\sigma_w M_w}{\rho_w R T} \quad (1b)$$

$$b = \frac{3 i m_s M_w}{4\pi \rho_w M_s} \quad (1c)$$

where s is the equilibrium saturation ratio of a solution droplet with radius r, σ_w is the surface tension of water, M_w is the molecular weight of water, R is the ideal gas constant, T is temperature in Kelvin, ρ_w is the density of water, and M_s is the molecular weight of the solute. The minimum saturation ratio that is required for spontaneous droplet growth, s_{act}, is therefore:

$$s_{crit} = 1 + \sqrt{\frac{4a^3}{27b}} \quad (2)$$

Petters and Kreidenweis [2007] reformulated the Köhler equation as κ-Köhler theory:

$$s_{crit} = exp\left(\sqrt{\frac{4A^3}{27 D_{act}^3 \kappa_{app}}}\right) \quad (3a)$$

and

$$A = \frac{4\sigma_{lv}M_w}{RT\rho_w} \quad (3b)$$

Where s_{crit} is the critical water vapor saturation ratio, D_{act} is the dry particle activation diameter and κ_{app} is the apparent hygroscopicity parameter. Solving for κ_{app} yields:

$$\kappa_{app} = \frac{4A^3\sigma_{lv}^3}{27T^3D_{act}^3 ln^2(s_{crit})} \quad (4)$$

The apparent hygroscopicity parameter can be calculated from experimental CCN results, where the dry diameter and water vapor saturation ratio are known. For a chosen aerosol diameter, the activated fraction is the ratio of the concentration aerosols that activate as CCN to the total aerosol concentration:

$$Activated\ fraction = \frac{CCN\ Concentration}{Aerosol\ Concentration} \quad (5)$$

Activated fraction data is fit with a sigmoid error function to determine the percent supersaturation at which 50 % of the particles have activated as CCN (activated fraction = 0.50), which is considered the operationally defined critical percent supersaturation SS_{crit} (Rose et al., 2008). The critical saturation ratio s_{crit} can then be determined and entered into Eq. (4) in order to calculate κ_{app} for the near-monodisperse aerosol:

$$s_{crit} = 1 + \frac{SS_{crit}}{100} \quad (6)$$

Reporting κ_{app} as a function of diameter allows for the comparison of the cloud condensation nucleation abilities of multimodal aerosol populations, without overlooking differences which arise due to aerosol composition.

The apparent hygroscopicity parameter is related to chemical composition; therefore, the calculated κ_{app} of a pure substance should be constant across CCN experiments. However, discrepancies between κ_{app} for a single chemical species have been observed. Experimental results for ammonium nitrate are inconsistent with reported values ranging from $0.577 \leq \kappa_{app} \leq 0.753$ (Svenningsson et al., 2006). Also, large ranges are often observed for organic compounds, such as glutaric acid ($0.054 \leq \kappa_{app} \leq 0.16$) and malonic acid ($0.199 \leq \kappa_{app} \leq 0.255$) (Koehler et al., 2006; Kumar et al., 2003; Hartz et al., 2006). Below we evaluate potential sources of uncertainties in CCN measurements and the resulting uncertainties in κ_{app}.

3. Artifacts derived from sized CCN measurements

CCN measurements used for calculating apparent hygroscopicity from monodisperse aerosol require accurate operation of three instruments: the CCN, the differential mobility analyzer (DMA), and the condensational particle counter (CPC). The setup for laboratory CCN experiments is shown in Fig. 1. First, a polydisperse population of aerosols is generated by an atomizer and dried using a desiccant tube packed with silica gel. A near-monodisperse flow is obtained through size-selection in the DMA. The flow is then split between a CPC (which measures aerosol concentration) and a CCN counter (which measures the concentration of particles that activate as cloud condensation nuclei at a given percent supersaturation). Instrument artifacts will first be assessed separately for the DMA, CPC, and CCN counter. In the concluding section of the paper (and Fig. 10), the overall uncertainty due to the combination of these is presented and discussed.

We note that this study considers sized CCN measurements which may be used for the determination of κ_{app}. In contrast, a number of earlier CCN studies conducted on the full ambient aerosol population without sizing the aerosol (Jennings et al., 1996; Hudson and Xie, 1998; Modini et al., 2015; Duan et al., 2017; Schmale et al., 2018; Leng et al., 2013). While useful, such studies do not produce the data required for accurate determination of κ_{app} from the CCN measurements.

3.1 Artifacts derived from differential mobility analyzers

3.1.1 DMA operation and electrical mobility

Differential mobility analyzers used in atmospheric science include commercially available instruments from Grimm Aerosol Technik, TSI Incorporated, and MSP Corporation. They have also been custom built by a number of research groups (Mei et al., 2011;Barmpounis et al., 2016;Jokinen and Makela, 1997;Seol et al., 2000). All models allow for the selection of particles through electrical mobility, the ability of a particle to move through a medium (such as air) while acted upon by an electrical field. The DMA size-selects near-monodisperse aerosol from a polydisperse aerosol source, as shown in Fig. 2 (modeled after the Vienna-type long Differential Mobility Analyzer from Grimm Technologies). The electrical mobility Z_p of a particle with mobility diameter d_m can be calculated according to:

$$Z_p = \frac{neC_C(d_m)}{3\pi\eta d_m} \tag{7}$$

where n is the number of charges on the particle (assumed to be one in this study), e is the elementary unit of charge, η is the gas dynamic viscosity, and $C_C(d_m)$ is the Cunningham slip correction factor:

$$C_C(d_m) = 1 + \frac{2\lambda}{d_m}\left(\alpha_{CC} + \beta_{CC}\exp\left[-\frac{\gamma_{CC}}{2\lambda/d_m}\right]\right) \tag{8}$$

where λ is the mean free path (DeCarlo et al., 2004). For the Vienna-type long Differential Mobility Analyzer from Grimm Technologies, Inc. considered here, $\alpha_{CC} = 1.246$, $\beta_{CC} = 0.42$, and $\gamma_{CC} = 0.86$ (Grimm Aerosol Technik, 2009).

Particle-laden flow enters the differential mobility analyzer through the aerosol inlet (flow Q_a), and travels down the DMA column (inner radius r_1, outer radius r_2) with the clean air sheath flow Q_{sh}. Positively-charged particles are attracted by the negatively-charged inner electrode, to which voltage V_0 has been

applied. Ideally, selection of a voltage allows only particles of a specific mobility diameter to exit the DMA through the sample flow Q_s. All particles with larger diameter (lower Z_p) or smaller diameter (higher Z_p) will exit the DMA through the excess flow Q_e. In other words, Q_s would ideally consist only of aerosols with diameters equal to, or very nearly equal to, the selected diameter.

In reality, the aerosol flow that leaves the DMA through Q_s is polydisperse with a mobility distribution determined by instrumental parameters. A triangular approximation has been chosen as a model for this distribution, as particle inertia is negligible for the diameters considered in this study (Stratmann et al., 1997; Mamakos et al., 2007). The probability that a particle at the aerosol inlet will exit with the sampling flow is defined by transfer function $f\left(Z_p, Z_{p,mid}\right)$:

$$f\left(Z_p, Z_{p,mid}\right) = \frac{\alpha_{TF}}{2\beta_{TF}}\left(\left|\frac{Z_p}{Z_{p,mid}} - (1+\beta_{TF})\right| + \left|\frac{Z_p}{Z_{p,mid}} - (1-\beta_{TF})\right| - 2\left|\frac{Z_p}{Z_{p,mid}} - 1\right|\right) \quad (9)$$

where $Z_{p,mid}$ is the midpoint mobility of the transfer function, and α_{TF} and β_{TF} are flow-derived constants, defined as:

$$\alpha_{TF} = \frac{Q_s + Q_a}{2Q_a} \quad (10a)$$

and

$$\beta_{TF} = \frac{Q_s}{Q_{sh}} \quad (10b)$$

The midpoint and half-width of the transfer function are respectively calculated according to: (Knutson and Whitby, 1975)

$$Z_{p,mid} = \frac{Q_e + Q_{sh}}{4\pi L V_0} \ln\left(\frac{r_2}{r_1}\right) \quad (11a)$$

and

$$\Delta Z_p = \frac{Q_a}{2\pi L V_0} \ln\left(\frac{r_2}{r_1}\right) \quad (11b)$$

where L is the distance between the DMA inlet and outlet.

3.1.2 κ_{app} artifacts arising from DMA flow ratios

Next we assess the ramifications of the DMA transfer function for the derived κ_{app}. A lognormal theoretical aerosol number distribution was used to represent a polydisperse ambient aerosol population (Fig. 3a). This distribution was converted to an electrical mobility distribution using Eq. (7) and Eq. (8), assuming that the aerosols in the distribution were spherical and singly charged. From the distribution, a series of single aerosol sizes were selected (25, 50, 100, and 200 nm diameter). For each aerosol size, the resulting DMA transfer functions were calculated for seven cases using Eq. (9) and the various parameters for DMA sheath, excess, aerosol, and sample flow listed in Table 1. These seven cases were chosen to represent possible measurements scenarios that may be encountered in a CCN experiment. The aerosol/sheath ratio is varied in Cases 1-4 in order to study the effects of chosen experimental parameters. Sheath flow is predetermined in some DMAs (for example, the Grimm Vienna DMA considered in this study), but can be varied in other instruments. The aerosol flow rate may also be selected in an experiment. Cases 5-7 vary the excess/sheath ratio in order to take proper instrument operation into account. The excess and sheath flow should be identical, but small discrepancies may occur.

For example, the resulting DMA transfer functions for a 100 nm aerosol conditions constrained by Cases 1-4 are shown in Fig. 3b, where an increase in Q_a/Q_{sh} from 0.1 (black line) to 0.3 (green line) tripled the width of the number distribution, and decreasing Q_a/Q_{sh} to 0.05 (blue line) from 0.10 halved the width of the number distribution. The result of applying the transfer functions shown in Fig. 3b to the distribution in Fig. 3a is shown in Fig. 3c.

All downstream distributions for all seven DMA cases and all aerosol sizes are shown in Fig. S1 in the Supplement. DMA Cases 1-4 represent experimental conditions in which the sheath and excess air flows are equal and the aerosol/sheath flow ratio is varied. As Q_a/Q_{sh} increases, the width of the number distribution measured downstream of the DMA increases, while the midpoint diameter remains constant. It was found that doubling the aerosol to sheath ratio doubled the width of the downstream number distribution for 25, 50, 100, and 200 nm particles. For example, when selecting 200 nm particles, increasing Q_a/Q_{sh} from 0.10 to 0.20 increased the downstream diameter range from 181-222 nm (a spread of 41 nm) to 167-250 nm (a spread of 87 nm). The particle diameter ranges that would be observed downstream of the DMA are summarized in Table 2.

To assess the variations in CCN properties resulting from DMA uncertainties the critical percent supersaturation were calculated for representative atmospheric aerosols. The value of SS_{crit} was calculated for each particle diameter using Eq. (3a), using literature values for apparent hygroscopicity of 0.61 for ammonium sulfate and 1.28 for sodium chloride (Clegg et al., 1998). It should be noted that this analysis considers two homogeneous aerosol distributions of hygroscopic salts. Real aerosol distributions tend to be mixtures of many species, and the shape of the number distribution can vary between species.

Note that in the absence of DMA diameter uncertainty, this single component aerosol population should be characterized by a single κ_{app} regardless of diameter. To test how uncertainties in DMA diameter translate to uncertainties in κ_{app}, the true critical saturation ratio s_{crit} was then put into Eq. (4) in order to calculate the "perceived" κ_{app} for each diameter given the chosen transfer function from Cases 1-7. For example, if 100 nm particles were selected from the DMA by the user, the transfer functions would allow larger and smaller particles to pass into the sample flow, as shown in Table 2. Particles with diameter > 100 nm would be "perceived" to have higher apparent hygroscopicity than particles with diameter < 100 nm, since the equilibrium vapor pressure over the surface of a particle decreases as its diameter increases (and as curvature decreases). Using Eq. (12), these diameter-specific "perceived" κ_{app} values were volume-weighted, resulting in $\kappa_{app,theory}$:

$$\kappa_{app,theory} = \sum_i \epsilon_i \kappa_i \quad (12)$$

where ϵ_i is the volume fraction of aerosol of each diameter i, and κ_i is the perceived κ_{app} for each diameter (adapted from Petters and Kreidenweis [2007]). Results for ammonium sulfate and sodium chloride are shown in Fig. 4a. The critical saturation ratio was calculated from $\kappa_{app,theory}$ using Eq. (3a) for each case and converted to critical percent supersaturation. The results are compared to theoretical κ-Köhler theory curves for ammonium sulfate and sodium chloride generated using the literature κ_{app} for each compound (Fig. 4b).

Discrepancies between $\kappa_{app,theory}$ calculated in this study and literature values (hereon referred to as "κ_{app} artifacts") are shown for both compounds in Fig. 4c-d.

The greatest κ_{app} artifacts were found in DMA case 4 (where the aerosol/sheath ratio was the highest) for both ammonium sulfate and sodium chloride aerosols. The artifacts for ammonium sulfate in DMA case 4 were 0.05-0.08, or 8-13 % of the literature value used for $\kappa_{app}^{(NH_4)_2SO_4}$, while the sodium chloride artifacts in DMA case 4 were 0.11-0.18, or 9-14 % of the literature value used for κ_{app}^{NaCl}. Artifacts were also high for DMA case 6 ($-0.025 \leq \kappa_{app,artifact}^{(NH_4)_2SO_4} \leq -0.018$) and DMA case 7 ($0.016 \leq \kappa_{app,artifact}^{(NH_4)_2SO_4} \leq 0.017$), where sheath and excess flow were unequal. This result demonstrates that artifacts may still occur when low aerosol/sheath flow ratios are chosen (0.15 and 0.08 for DMA cases 6 and 7, respectively) due to small differences between sheath and excess flow rates (5% and 2% for DMA cases 6 and 7, respectively).

κ_{app} artifacts were larger for sodium chloride ($-0.05 \leq \kappa_{app,artifact}^{NaCl} \leq 0.18$,$4 - 14$ % of κ_{app}^{NaCl}) than for ammonium sulfate ($-0.03 \leq \kappa_{app,artifact}^{(NH_4)_2SO_4} \leq 0.08$, $5 - 13$ % of $\kappa_{app}^{(NH_4)_2SO_4}$) across the DMA cases. As our results show, when two or more compounds are compared, the more hygroscopic compound will have larger κ_{app} artifacts.

3.1.3 Effect of double and triple charges on particles

During normal operation, the Grimm DMA employs a bipolar charger (also known as a neutralizer) to charge aerosol particles through the capture of gaseous ions. The analysis in Section 3.1.2 assumes that each particle carries a single (+1) charge. In reality, the methods used to charge particles prior to entering a DMA may impart two, three, or more charges to individual particles (Fuchs, 1963). The charge distribution resulting from a bipolar charger is roughly approximated using the Boltzmann law

(Keefe et al., 1959). However, the Boltzmann law assumes symmetric aerosol particle charging (equal concentrations of negatively and positively charged particles). Deviation from symmetric charging is observed in regions of high ionizations, and this deviation becomes more pronounced as particle size increases (Hoppel and Frick, 1990).

A more accurate estimation of stationary charge distribution has been calculated using an approximation formula for the charge distribution produced by a bipolar charger:

$$f(k) = 10^{\left[\sum_{i=0}^{i=5} a_i(k)(\log_{10} D_{nm})^i\right]} \quad (13)$$

where $f(k)$ is the fraction of particles carrying k charges, $a_i(k)$ are approximation coefficients determined using a least-squares regression analysis, and D_{nm} is the particle diameter in nanometers (Wiedensohler, 1988). The approximation coefficients only apply to particles with 0, ±1, and ±2 charges. In a separate study, **Maricq et al., 2008** determined approximation coefficients for poly (α-olefin) oligomer oil droplets with ±1, ±2, and ±3 charges. The approximation coefficients reported by these two studies were in excellent agreement for particles with ±1 and in weak agreement for ±2 charges (+2 and -2 charging efficiencies were overestimated by 50% and 100%, respectively). Therefore, this analysis will use the approximation coefficients from Wiedensolher, 1988 for particles with +1 and +2 charges, and the approximation coefficient for particles with +3 charge from Maricq et al., 2008.

In order to assess the impact of multiple charges on κ_{app}, Eq. (13) and the approximation coefficients from Wiedensolher, 1988 and Maricq et al., 2008 were used to calculate the charge distribution of the representative aerosol population shown in Fig. 3a. The resulting charge distribution is shown in Fig.

S2a. An increase in multiple charging is observed as particle diameter increases, though this is offset somewhat by the decrease in concentration with particle size above 50 nm.

It follows that aerosols incorrectly sized due to double and triple changing will be passed from the DMA to the CCN and result in an additional uncertainty in the CCN measurements. To illustrate this, activated fraction curves, were generated for 25, 50, 100, and 200 nm sodium chloride particle selection by the DMA (Fig. 5). The activation of sodium chloride is represented by sigmoid curves, where the midpoint of each activation curve is the κ-Köhler-derived critical supersaturation of sodium chloride, and the standard deviation of each curve is one-tenth of this value (consistent with the standard deviation/midpoint ratio observed from our instrument's ammonium sulfate CCN calibration data). For each particle diameter, D, the observed activated fraction, $AF_{D,weighted}^{SS}$, for each percent supersaturation SS was determined by weighting the activated fraction $AF_{D,i}^{SS}$ of each particle diameter/charge at that percent supersaturation, by the fraction of particles of that diameter:

$$AF_{D,weighted}^{SS} = \sum_{i=1}^{i=3} \frac{concentration\ of\ particles\ with\ charge\ i\ and\ diameter\ D}{concentration\ of\ particles\ with\ charge{+}1{,+}2{,+}3{,and\ diameter\ D}} AF_{D,i}^{SS} \quad (14)$$

The raw data shown in Fig. 5 (green curves) can be corrected for multiple charging by determining the fraction of particles with > +1 charge from the lower plateau in each plot (dashed lines). The adjusted activated fraction for each percent supersaturation, $AF_{adjusted}$, is calculated using the equation:

$$AF_{adjusted} = \frac{AF_{raw} - AF_{plateau}}{1 - AF_{plateau}} \quad (15)$$

where AF_{raw} is the raw activated fraction at that percent supersaturation, and $AF_{plateau}$ is the activated fraction corresponding to the lower plateau (Rose, 2008). The adjusted activated fraction curves are shown in Fig. 5 (blue curves). These are in good agreement with the theoretical κ-Köhler-derived activation curves for sodium chloride (not shown).

Critical supersaturation was determined for each diameter by calculating the percent supersaturation at which the raw $AF_{D,weighted}^{SS} = 0.5$. These critical supersaturations are shown in Fig. 6a, and the theoretical critical supersaturations calculated from κ-Kohler theory are shown for comparison. Eq. 4 was used to calculate apparent hygroscopicity for each particle diameter, shown in Fig. 6b. A dashed line in Fig. 6b indicates the literature value for κ_{app}^{NaCl}. It is apparent that failing to account for multiply-charged particle in the activated fraction curves shown in Fig. 5 leads to an overestimation of κ_{app}. Artifacts in κ_{app} are shown in Fig. 6c.

For the theoretical aerosol distribution used in this analysis (Fig. 3a), small, positive deviations from κ-Köhler theory and the literature value for κ_{app}^{NaCl} were observed ($0.01 \leq \kappa_{app,artifact}^{NaCl} \leq 0.04, 1 -$ 3 % of κ_{app}^{NaCl}). As shown in the figure, κ_{app} artifacts resulting from unaccounted-for multiple charges decrease with particle diameter for this theoretical aerosol population. Greater κ_{app} artifacts would be expected for aerosol populations with more prevalent accumulation modes.

The aerosol/sheath ratio within the DMA also modulates the effect of multiple charges on κ_{app}. As the aerosol/sheath ratio increases, the transfer function broadens, allowing particles that are both larger and smaller than the selected diameter to exit the DMA. This in turn broadens the CCN activated fraction curve (Rose et al., 2008). The larger particles will activate as CCN at lower supersaturations than

particles with the selected diameter, resulting in an increase in the activated fraction plateau due to multiple-charged particles and a further decrease in the determined SS_{crit}. Petters et al. 2007b showed that CCN activated fraction curves are significantly skewed by multiply-charged particles when the mode diameter of the aerosol population upstream of the DMA exceeds the critical diameter of the size-selected particles. In an example CCN activated fraction curve, Rose et al. 2008 demonstrated that a 1:6 ratio of doubly-to-singly charged particles resulted in an underestimation of the critical activation diameter by 2%. Zhao-Ze and Liang, 2014 also showed that multiply-charged particles can introduce significant uncertainty into hygroscopicity calculations.

3.1.4 Additional artifacts resulting from DMA measurements

Several additional factors that may impact experimental κ_{app} are beyond the scope of this study, but are worth mentioning as they represent additional potential sources of error in some cases. First, volatile aerosols may partially evaporate inside the DMA, resulting in a decrease in particle size exiting the DMA. DMA sizing error due to aerosol volatility (defined as the ratio of sampled diameter to the selected diameter) increases with volatility, though sizing error can be decreased by increasing the sheath flow rate in the DMA. Conversely, hygroscopic aerosols may grow inside the DMA, resulting in larger particles existing the DMA. Operationally, errors in DMA sizing due to hygroscopic growth can be mitigated if aerosols entering the DMA inlet are in wet metastable states (higher aerosol RH at DMA inlet), and if DMA sheath flow rates are kept low (Khlystov, 2014).

Voltage shifts within the DMA (differences between the selected voltage and the actual voltage inside the DMA) can lead to discrepancies between selected and sampled particle diameters. Voltage shifts may result from a space-charge field generated by the motion of charges within the DMA. Particles

charged by the bi-polar neutralizer will either be attracted towards or repelled away from the inner column of the DMA, depending on whether they are positively or negatively charged. This charge separation creates a space-charge field which shifts the actual voltage within the DMA from the selected voltage. The impact of the space-charge field on the midpoint and spread of the DMA transfer function increases as particle mobility increases (as particle size decreases), and as particle concentration increases (Alonso and Kousaka, 1996; Alonso et al., 2000; Alonso et al., 2001).

4. Artifacts derived from condensation particle counters

4.1 CPC operation at low concentration

The second instrument which must function accurately during CCN experiments is the condensation particle counter. CPC performance is characterized by the maximum counting efficiency (which may be influenced by the working fluid in the instrument) and the 50 %-cut-off diameter (d_{50}), the particle diameter at which 50 % counting efficiency is observed, both of which can vary between commercially available models and even between individual CPCs (Heim et al., 2004). One study found that n-butanol CPCs (TSI, Inc. Models 3772, 3775, and 3776) exhibited smaller d_{50} for silver particles than sodium chloride ($3.3\ nm \leq d_{50}^{Ag} \leq 7.8\ nm$ and $4.1\ nm \leq d_{50}^{NaCl} \leq 14.7\ nm$), due to the more effective condensation of n-butanol on silver particles (Hermann et al., 2007).

Maximum counting efficiencies in that study varied from 88.9 % to 100.3 %. Another comparison of n-butanol CPCs (TSI Inc. Models 3010 and 3022, Grimm Tech. Inc. Model 5.403) found $3.1\ nm \leq d_{50} \leq 11.9\ nm$ for sodium chloride aerosols (Heim et al., 2004). In another study, the counting efficiencies observed in measurements of tungsten oxide particles by different instruments of the same model (TSI 3025) varied from 88.9 % to 138.9 %, while $d_{50}^{WO_x}$ varied from 3.2 nm to 11.0 nm (Hameri et al., 2002).

While some issues can cause undercounting at all concentrations, the additional issue of uncounted particles due to the arrival of more than one particle in the detector's field of view at any time arises only at higher concentrations. The cut-off between "low" and "high" concentration is not exact and varies between instruments. CPC undercounting issues which arise even at relatively low concentrations (which one would expect to encounter under standard experimental conditions) will be discussed in this

section. Concentration-dependent effects encountered at higher concentrations will be explored in Sect. 4.2.

Six counting efficiency curves were generated using sigmoidal distributions and the 50 % cut-off diameters and maximum counting efficiencies listed in Table 3. Chosen values represent d_{50} values and maximum counting efficiencies reported in the literature under relatively low concentrations of 1000-4000 cm^{-3} (Hermann et al., 2007). The resulting sigmoidal distributions (Fig. 7a) were used to determine the counting efficiency of 25, 50, 100, and 200 nm particles.

Next, κ_{app} was calculated from theoretical critical percent supersaturations for each chosen diameter. To do so, four sigmoid curves representing sodium chloride CCN activation (hereon referred to as "activation curves") for 25, 50, 100, and 200 nm were generated. The κ-Köhler-SS_{crit} of sodium chloride was used as the midpoint of each activation curve, and one-tenth of this value was used as the standard deviation (100 % CE, Fig. 7b-e). These values are consistent with the standard deviation/midpoint ratio observed from our instrument's ammonium sulfate CCN calibration data.

Activation curves were then generated for CPC Cases 1-6 by dividing the activated fraction for each dry particle diameter by the counting efficiency for that diameter. SS_{crit} was determined for each CPC case by finding the percent supersaturation at which activated fraction = 0.50. Results are summarized in Fig. 7f. Next, critical supersaturation was converted to saturation, and $\kappa_{app,theory}$ was calculated for each diameter in each CPC Case using Eq. (4) (see Fig. 7g). As above, κ_{app} artifacts were calculated by finding the difference between these results and the literature value of κ_{app} for sodium chloride (see Fig. 7h).

For the diameters studied, the effect of maximum counting efficiency on CPC concentration (and activated fraction) is greater than the effect of 50 %-cutoff diameter. However, neither characteristic resulted in large κ_{app} artifacts. The largest κ_{app} artifact observed at "low" concentrations was 0.035 for CPC Case 4, 2.4 % of the literature value for the apparent hygroscopicity factor for sodium chloride.

4.2 CPC operation at high concentration

Operation at high concentrations introduces an additional source of undercounting through particle coincidence at the CPC optical counter. For the TSI 3010 CPC, undercounting is observed is for particle concentrations above $1 \times 10^4\ cm^{-3}$. At $5 \times 10^4\ cm^{-3}$, the detector saturates and cannot detect higher concentrations. By comparison, the TSI 3025 is effective at counting higher particle concentrations, of up to $2.5 \times 10^4\ cm^{-3}$ (Hameri et al., 2002;Sem, 2002).

To model undercounting due to particle coincidence, four CPC counting curves (Fig. 8a) were generated using the equations in Table 4. Case 7 represents a CPC where counting efficiency decreases with particle concentration, without reaching saturation. Cases 8-10 represent CPCs where saturation is reached at $4 \times 10^4\ cm^{-3}$, $2 \times 10^4\ cm^{-3}$, and $1 \times 10^4\ cm^{-3}$, respectively. These saturation concentrations are of similar magnitude to those observed from TSI 3010 concentration data. It should be noted that the CPC concentration in Cases 7-10 levels off at the saturation concentration for each case.

In order to assess the importance of undercounting in CPC Cases 7-10, four theoretical aerosol distributions with a peak concentration at 50 nm were employed (Table 5, Fig. 8b). CPC Distribution 1 represents a worst-case scenario of similar magnitude to the highest particle concentrations measured during a coastal nucleation event (Hameri et al., 2002; Sem, 2002), while CPC Distributions 2, 3, and 4 are lower in concentration (due to the lack of undercounting in CPC Distributions 2, 3, and 4 as demonstrated in Figure 6b, the remaining analysis for CPC operation at high concentration considers only CPC Distribution 1.) CPC Cases 8-10 were applied to CPC Distribution 1 in order to determine

the concentration measured by the CPC for 25, 50, 100 and 200 nm aerosols. The counting efficiency was then calculated for each case and aerosol diameter in CPC Distribution 1.

Sigmoidal activated fraction curves were generated for 25, 50, 100 and 200 nm sodium chloride aerosols. As in the low concentration cases, the midpoint of each 100 % CE curve was chosen to be equal to the κ-Köhler-derived SS_{crit} of sodium chloride at each dry diameter, and the standard deviation of each curve is equal to one-tenth of the SS_{crit}. These activated fraction curves were adjusted using the counting efficiencies calculated in the previous step. In cases where the activated fraction has increased due to undercounting by the CPC, the theoretical sigmoidal curve shifts to the left relative to the 100 % CE case (Fig. 8c-f). Thus, undercounting by the CPC effectively increases the reported activated fraction. As before, SS_{crit} was determined from each of these curves, and $\kappa_{app,theory}$ was subsequently calculated using Eq. (4) (Fig. 8g-h).

$\kappa_{app,theory}$ fell over a much wider range for 25, 50, and 100 nm particles (1.30-1.56, 1.32-1.70, and 1.30-1.55, respectively) than for 200 nm particles (1.28-1.29) due to the lower concentration of 200 nm particles in the chosen aerosol distribution, which resulted in a higher counting efficiency for these aerosols. In comparison, the largest range in $\kappa_{app,theory}$ was observed for 50 nm aerosols, the peak diameter in this aerosol distribution.

A wider range in $\kappa_{app,theory}$ was observed for the high-concentration CPC Cases (7-10) compared to the low-concentration CPC Cases (1-6). The lowest counting efficiency observed across the low-concentration cases was 89.9 % for 25 nm aerosol in Case 4, while the lowest counting efficiency observed in the high-concentration cases was 18.0 % for 50 nm aerosol in Case 10.

519 Artifacts in the apparent hygroscopicity parameter are shown in Fig. 8i. κ_{app} artifacts were the greatest
520 for a CPC that becomes saturated at 20,000 particles/cm^3 ($0.0131 \leq \kappa_{app} \leq 0.4206$). The lower the
521 concentration at which a CPC becomes saturated, the more quickly its counting efficiency will drop as
522 concentration increases, resulting in increased activated fraction and increased apparent hygroscopicity.
523 The magnitude of artifacts due to CPC undercounting depends on the saturation concentration of the
524 CPC and the distribution of the aerosol population being studied.

5. Artifacts derived from cloud condensation nuclei instruments

Finally, the third instrument whose performance accuracy contributes to the overall certainty in CCN assessment in the CCN instrument itself. Several instruments have been implemented for measuring CCN concentrations over the last few decades. Older models include the Continuous Flow Parallel Plate Diffusion Chamber (Sinnarwalla, 1973) and the Hudson CCN spectrometer (Hudson, 1989) which both employ an applied temperature gradient perpendicular to the aerosol flow. Newer models, such as the widely-used Droplet Measurement Technology Cloud Condensation Nuclei Counter (DMT CCN-100), operate with a streamwise temperature gradient and continuous, laminar flow (Lance et al., 2006). The following analysis considers the DMT CCN-100. According to the CCN-100 manual, the counting efficiency for this CCN instrument depends on concentration and supersaturation (Fig. 9a). The counting efficiency decreases rapidly with concentration at < 0.2 % SS due to rapid water vapor depletion at these low supersaturations, and falls off more slowly for > 0.2 % SS (DMT CCN-100 manual).

The counting efficiency of the DMT CCN-100 was tested for four lognormal aerosol distributions with peak concentrations at 50 nm and varying total concentrations (Table 5, Fig. 9b). Note that CCN Cases 1-4 are identical to the aerosol distributions CPC Distributions 1-4 used for the high-concentration CPC cases.

The counting efficiencies for each case were applied to theoretical sodium chloride sigmoidal activated fraction curves to produce normalized activated fraction curves (Fig. 9c-f). As above, the midpoint is set to the SS_{crit} of sodium chloride at each dry diameter, and the standard deviation is assumed to be one-tenth of SS_{crit}. CCN undercounting effectively decreases activated fraction, therefore shifting the

activated fraction curve downwards and towards higher percent supersaturations. The opposite effect is observed when CPC undercounting occurs. Critical supersaturation was determined for each CCN case, as above (Fig. 9g). Values of SS_{crit} were then converted to saturation, and $\kappa_{app,theory}$ was calculated using Eq. (4) (Fig. 9h).

Significant deviations from κ-Köhler theory were only observed in CCN Case 1, with total aerosol concentration 5×10^6 particles/cm^3 (Fig. 9g-i). The largest deviation for CCN Case 1 was observed in 100 nm particles ($\kappa_{app,artifact} = -0.57$), due to the higher concentration of 100 nm particles compared to 25 and 200 nm particles, and the lower percent supersaturation necessary for activation. The largest artifacts across CCN Cases 2 and 3 were also observed for 100 nm particles, though no artifacts were observed for any particle diameter in CCN Case 4 due to the much lower concentrations.

Sodium chloride is very hygroscopic. It should be noted that aerosols consisting of less hygroscopic compounds will activate at higher percent supersaturations (> 0.2 % SS regime) which will lead to smaller κ_{app} artifacts when the same aerosol distribution and total aerosol concentration is considered. If a mixture was considered (for example, sodium chloride with a non-hygroscopic species such as soot) the results may also be different. The shape of the aerosol distribution must also be taken into account. A distribution with a narrower peak than the one generated for this analysis would be at risk for larger κ_{app} artifacts for any total aerosol concentration, and these artifacts would be greater at the peak diameter, while a broader distribution would result in less variation in κ_{app} artifacts for each particle diameter.

6. Counting statistics in CCN and CPC measurements

Though it is beyond the scope of this analysis, it should be mentioned that sampling at very low particle concentrations (< 200 cm^{-3} total particle concentration) can introduce additional error into CCN and CPC measurements. This error can be mitigated by increasing scan times (Moore et al., 2010). For example, Moore et al., 2010 averaged CCN and particle concentrations over 5-second intervals for monodisperse particle concentrations < 10 cm^{-3}, and increased averaging time to 20-second intervals when the monodisperse particle concentration reached < 6 cm^{-3}.

7. Discussion

A comparison of several instrument sources of error in CCN-derived κ_{app} is shown in Fig. 10. In addition, the best and worst case combination of errors, determined by additive error propagation, are also shown. DMA Case 4, CPC Case 4, CPC Case 10, and CCN Case 1 represent the operating conditions that resulted in the largest κ_{app} artifacts in this study. In DMA Case 4, the aerosol/sheath ratio of 0.30 resulted in a broadened aerosol distribution downstream of the DMA. Compared to DMA Case 1, where $Q_a/Q_{sh} = 0.10$, the downstream diameter range in DMA Case 4 was 300 % higher for 25 nm particles, resulting in a spread of 20-36 nm. Similarly, the diameter ranges for 50, 100, and 200 nm diameter were 220 %, 230 %, and 220 % wider than in Case 1, respectively. Compared to the most ideal DMA case presented in this study (DMA Case 2), where $Q_a/Q_{sh} = 0.05$, the downstream diameter range in DMA Case 4 was 700 % higher for 25 nm particles; the diameter ranges for 50, 100, and 200 nm diameter were 540 %, 560 %, and 520 % wider than in Case 2, respectively. The results demonstrate that limiting Q_a/Q_{sh} to ≤ 0.10 will result in a narrow particle size distribution downstream of the DMA. Other studies have recommended employing DMA sample/sheath ratios of 0.2 (Petters et al., 2007; Carrico et al., 2008; Moore et al., 2010) or 0.1 (Moore et al., 2010; Zhao-Ze and Liang, 2014) in order to minimize measurement aerosols due to transfer function broadening.

The effects of multiply-charged particles on κ_{app} calculations were also quantified, as shown in Fig. 10. Small, positive κ_{app} artifacts ($1 - 3$ % of κ_{app}^{NaCl}) were observed when particles with +2 and +3 charges were not accounted for. This analysis considered a theoretical aerosol distribution in which most of the particles measure less than 100 nm in diameter. Actual aerosol distributions vary temporally and spatially, and often include accumulation and coarse modes that would result in larger κ_{app} artifacts.

CPC Case 4 represents κ_{app} artifacts (0.031-0.035) due to undercounting that arises from poor maximum CPC counting efficiency (90 %), which may be observed when using butanol as a working fluid while measuring the concentration of inorganic aerosols. In contrast, κ_{app} artifacts are negligible (< 0.10 % of κ_{app}^{NaCl}) in CPC Case 3, where maximum counting efficiency = 100 %. CPC Cases 8 and 10 (applied to the highest-concentration case, CPC Distribution 1) represent undercounting at high concentration with CPCs where saturation is observed at $4 \times 10^4\ cm^{-3}$ and $1 \times 10^4\ cm^{-3}$, respectively. Counting efficiency drops off more rapidly with concentration in the latter case, resulting in κ_{app} artifacts that are highest at the peak of the aerosol distribution (0.1190 and 0.4206 for 50 nm aerosols in CPC Cases 8 and 10, respectively). It should be noted that undercounting was only observed for one of the four upstream distributions studied, CPC Distribution 1. No undercounting was observed when CPC Cases 7-10 were applied to CPC Distributions 2-4.

CCN Case 1 represents CCN undercounting at high concentration (total aerosol concentration = $5 \times 10^6 cm^{-3}$). CCN undercounting is greatest for low supersaturation (< 0.2 %) and high concentration, resulting in the lowest counting efficiency and highest κ_{app} artifacts (- 0.57) for 100 nm aerosols in CCN Case 1. The largest CCN-derived κ_{app} artifact observed outside of CCN Case 1 was – 0.01 for 100 nm aerosols in CCN Case 2.

The combined artifacts for the cases where the highest artifacts were observed (DMA Case 4, multiple particle charging, CPC Case 4, CPC Case 10, CCN Case 1) are 0.21, 0.24, 0.32, and 0.21 for 25, 50, 100, and 200 nm particles respectively, as shown in Fig. 10. The combined artifacts for the lowest-artifact cases (DMA Case 2, CPC Case 3, and CCN Case 4) are < 0.001 except for 200 nm particles, where $\kappa_{app,artifact}$ = 0.0013.

We note that Fig. 4c-d demonstrated that κ_{app} error may result from instrument artifacts for ammonium sulfate and sodium chloride, two standard compositions used in calibration of CCN instruments (Rose et al., 2008). Therefore, the κ_{app} error encountered while calibrating the CCN instrument may compensate for the CCN measurement bias of aerosol samples. However, as also demonstrated in Fig. 4c-d, the magnitude of this instrumentally-derived bias varies by compound.

Conclusions

The sensitivity of weather and climate models to accuracy in CCN activation predictions has been demonstrated in other works. Possible sources of apparent hygroscopicity artifacts calculated from CCN measurements have been presented in this study. This analysis has focused on sodium chloride and ammonium sulfate aerosols, but it can be extended to other aerosol populations, including mixtures and field samples.

The greatest combined artifacts ($0.22 < \kappa_{app,artifact} < 0.34$, NaCl) occurred as a result of the combined issues of the highest DMA aerosol/sheath ratio, uncorrected multiple particle charging, and undercounting by both CPC and CCN instrument. The lowest combined artifacts ($0.00018 < \kappa_{app,artifact} < 0.0013$, NaCl) occurred as a result of ideal operating conditions :lowest DMA/sheath ratio, corrected multiple particle charging, and little to no undercounting.

The largest single-instrument artifacts ($-0.57 < \kappa_{app,artifact} < 0.42$ for sodium chloride) in this study arise from undercounting by either the CPC or CCN counter at high concentration. This problem arises during attempts to measure aerosol concentrations of ~10^4 cm^{-3} which is much higher than the recommended concentration ranges for either instrument, (CPC Cases 7-10 and CCN Case 4). Corrective action should be taken to dilute aerosol samples in order to avoid undercounting. It should be noted that these artifacts are for individual instruments and do not take combined operation of the CPC and CCN into account; when both instruments undercount, artifacts in $\kappa_{app,artifact}$ are reduced.

Smaller single-instrument artifacts ($\kappa_{app,artifact} < 0.04$) were observed for the CPC cases where 50 %-cut-off diameter and maximum counting efficiency were varied. Given the chosen particle diameters

(25, 50, 100, 200 nm), κ_{app} artifacts due to d_{50} were minimal. The largest κ_{app} artifacts for a CPC counting at low concentration (0.031-0.035) were observed where the maximum counting efficiency was equal 0.90. This may represent a compositional mismatch between n-butanol as the working fluid and sodium chloride as the aerosol, due to the poor solubility of the latter in the former. Individual n-butanol CPCs may exhibit higher maximum counting efficiencies for sodium chloride.

Uncertainty arising from the DMA depended greatly on the chosen aerosol and sheath settings. One set of DMA cases (Cases 2-4) examined the effect of aerosol/sheath ratio. By decreasing this ratio, a narrower near-monodisperse flow can be produced, which increases the accuracy of calculated κ_{app}. The κ_{app} artifacts for an aerosol/sheath ratio of 0.10 were 1.1 % of $\kappa_{literature}$ for 25 nm sodium chloride aerosols, 0.93 % for 50 nm, 0.81 % for 100 nm, and 0.66 % for 200 nm. Decreasing the aerosol/sheath ratio to 0.05 resulted in $\kappa_{app} \approx 0.01$ % of $\kappa_{literature}$ for NaCl. When a ratio of 0.30 was employed, the resulting artifacts that were ~10 % of $\kappa_{literature}$ for sodium chloride.

The second set of DMA cases (5-7) were designed to evaluate the effects of holding the sheath flow constant while varying the excess air flow by -2 %, +2 %, and +5 %. These resulted in shifts of ≤ 2 nm for 25 nm and 50 nm particles, ≤ 4 nm for 100 nm particles, and ≤ 7 nm for 200 nm particles. The downstream aerosol distribution was shifted towards larger particle diameters when sheath flow exceeded excess flow, and towards smaller particle diameter when sheath flow was less than excess flow. When taking field measurements, the composition of the sample may vary with particle diameter, thereby introducing another source of error from a broader DMA distribution.

Under optimal operating conditions, where the DMA sample/sheath ratio is 0.10 and excess/sheath ratio is 1.0, and in the absence of undercounting by the CPC or CCN, uncertainties in κ_{app} are within ±1.1 %

for 25 to 200 nm particles. When the DMA sample/sheath ratio drops to 0.05, κ_{app} uncertainties decrease to ±0.01 %. Additionally, errors in activated fraction (and therefore κ_{app}) resulting from the bipolar charge distribution can be corrected by determining the fraction of particles with multiple charges.

Apparent hygroscopicity parameter artifacts were calculated for two pure, inorganic species in this study. This analysis could be used to estimate κ_{app} artifacts for ambient aerosol populations, which may result in a better understanding of the "real' differences between these populations. As discussed in the introduction, Collins et al. 2016 aggregated κ_{app} from several mesocosm and field studies for 30-100 nm sea spray aerosol ($0.4 < \kappa_{app}^{SSA} < 1.3$). The wide range of κ_{app} in these studies may be attributed to differences in composition, experimental artifacts, or a combination of the two. Quantification of experimental artifacts would facilitate interpretation of κ_{app} in aerosol populations and constrain the importance of composition in CCN activation. There has been a recent proliferation of CCN data availability from multiple researchers and multiple experimental setups. To maximize the utility of these studies and to compare cloud-activating properties of various ambient aerosol masses, it is essential that artifacts are considered in both CCN data collection and in reporting of the data.

Supplement Link

Will be included by Copernicus

Author Contribution

Sarah D. Brooks provided the conceptual framework and contributed to the writing of the manuscript. Jessica A. Mirrielees performed the analysis and lead the writing of the manuscript.

Competing Interests

The authors declare that they have no conflict of interest.

Disclaimer

Will be included by Copernicus

Acknowledgements

This project was supported by the National Science Foundation of the United States (Award #15398810). In addition, Mirrielees thanks Texas A&M University for support through Institute for and Advanced Studies HEEP PhD Fellowship and a Lechner Scholarship.

References

Alonso, M., and Kousaka, Y.: Mobility shift in the differential mobility analyzer due to Brownian diffusion and space-charge effects, J. Aerosol. Sci., 27, 1201-1225, 10.1016/0021-8502(96)00052-3, 1996.

Alonso, M., Alguacil, F. J., and Kousaka, Y.: Space-charge effects in the differential mobility analyzer, J. Aerosol. Sci., 31, 233-247, 10.1016/s0021-8502(99)00051-8, 2000.

Alonso, M., Alguacil, F. J., Watanabe, Y., Nomura, T., and Kousaka, Y.: Experimental evidence of DMA voltage shift due to space-charge, Aerosol Sci. Technol., 35, 921-923, 10.1080/02786820126855, 2001.

Asa-Awuku, A., Nenes, A., Gao, S., Flagan, R. C., and Seinfeld, J. H.: Water-soluble SOA from Alkene ozonolysis: composition and droplet activation kinetics inferences from analysis of CCN activity, Atmos. Chem. Phys., 10, 1585-1597, 10.5194/acp-10-1585-2010, 2010.

Andreae, M. O., and D. Rosenfeld. 2008. "Aerosol-cloud-precipitation interactions. Part 1. The nature and sources of cloud-active aerosols." Earth-Science Reviews 89 (1-2):13-41. doi: 10.1016/j.earscirev.2008.03.001.

Barmpounis, K., Maisser, A., Schmidt-Ott, A., and Biskos, G.: Lightweight differential mobility analyzers: Toward new and inexpensive manufacturing methods, Aerosol Sci. Technol., 50, 4, 10.1080/02786826.2015.1130216, 2016.

Betancourt, R. M., Nenes, A., and Liu, X. H.: Relative Contributions of Aerosol Properties to Cloud Droplet Number: Adjoint Sensitivity Approach in a GCM, in: AIP Conference Proceedings, 19th International Conference on Nucleation and Atmospheric Aerosols (ICNAA), Colorado State Univ, Ctr Arts, Fort Collins, CO, 2013, WOS:000319766400170, 679-682, 2013.

Betancourt, R. M., and Nenes, A.: Understanding the contributions of aerosol properties and parameterization discrepancies to droplet number variability in a global climate model, Atmos. Chem. Phys., 14, 4809-4826, 10.5194/acp-14-4809-2014, 2014.

Bougiatioti, A., Fountoukis, C., Kalivitis, N., Pandis, S. N., Nenes, A., and Mihalopoulos, N.: Cloud condensation nuclei measurements in the marine boundary layer of the eastern Mediterranean: CCN closure and droplet growth kinetics, Atmos. Chem. Phys., 9, 7053-7066, 10.5194/acp-9-7053-2009, 2009.

Brooks, S. D., and Thornton, D. C. O.: Marine Aerosols and Clouds, in: Annual Review of Marine Sciences, Vol 10, edited by: Carlson, C. A., and Giovannoni, S. J., Annual Review of Marine Science, 289-313, 2018.

Carrico, C. M., Petters, M. D., Kreidenweis, S. M., Collett, J. L., Engling, G., and Malm, W. C.: Aerosol hygroscopicity and cloud droplet activation of extracts of filters from biomass burning experiments, J. Geophys. Res.-Atmos., 113, 9, 10.1029/2007jd009274, 2008.

Carslaw, K. S., Lee, L. A., Reddington, C. L., Pringle, K. J., Rap, A., Forster, P. M., Mann, G. W., Spracklen, D. V., Woodhouse, M. T., Regayre, L. A., and Pierce, J. R.: Large contribution of natural aerosols to uncertainty in indirect forcing, Nature, 503, 67-+, 10.1038/nature12674, 2013.

Chang, D. Y., Lelieveld, J., Tost, H., Steil, B., Pozzer, A., and Yoon, J.: Aerosol physicochemical effects on CCN activation simulated with the chemistry-climate model EMAC, Atmospheric Environment, 162, 127-140, 10.1016/j.atmosenv.2017.03.036, 2017.

Clegg, S. L., Brimblecombe, P., and Wexler, A. S.: Thermodynamic model of the system H+-NH4+-SO42--NO3--H2O at tropospheric temperatures, J. Phys. Chem. A, 102, 2137-2154, 10.1021/jp973042r, 1998.

Collins, D. B., Bertram, T. H., Sultana, C. M., Lee, C., Axson, J. L., and Prather, K. A.: Phytoplankton blooms weakly influence the cloud forming ability of sea spray aerosol, Geophys. Res. Lett., 43, 9975-9983, 10.1002/2016gl069922, 2016.

760 Crosbie, E., Youn, J. S., Balch, B., Wonaschutz, A., Shingler, T., Wang, Z., Conant, W. C., Betterton, E.
761 A., and Sorooshian, A.: On the competition among aerosol number, size and composition in predicting
762 CCN variability: a multi-annual field study in an urbanized desert, Atmos. Chem. Phys., 15, 6943-6958,
763 10.5194/acp-15-6943-2015, 2015.
764 DeCarlo, P. F., Slowik, J. G., Worsnop, D. R., Davidovits, P., and Jimenez, J. L.: Particle morphology
765 and density characterization by combined mobility and aerodynamic diameter measurements. Part 1:
766 Theory, Aerosol Sci. Technol., 38, 1185-1205, 10.1080/027868290903907, 2004.
767 Duan, J. Y., Tao, J., Wu, Y. F., Cheng, T. T., Zhang, R. J., Wang, Y. Y., Zhu, H. Y., Xie, X., Liu, Y. H.,
768 Li, X., Kong, L. D., Li, M., and He, Q. S.: Comparison of aerosol and cloud condensation nuclei
769 between wet and dry seasons in Guangzhou, southern China, Sci. Total Environ., 607, 11-22,
770 10.1016/j.scitotenv.2017.06.246, 2017.
771 Fitzgerald, J. W.: Approximation formulas for equilibrium size of an aerosol particle as a function of its
772 dry size and composition and relative humidity, Journal of Applied Meteorology, 14, 1044-1049,
773 10.1175/1520-0450(1975)014<1044:afftes>2.0.co;2, 1975.
774 Fitzgerald, J. W., Hoppel, W. A., and Vietti, M. A.: The size and scattering coefficient of urban aerosol
775 partices at Washington, DC as a function of relative humidity, Journal of the Atmospheric Sciences, 39,
776 1838-1852, 10.1175/1520-0469(1982)039<1838:tsasco>2.0.co;2, 1982.
777 Hameri, K., O'Dowd, C. D., and Hoell, C.: Evaluating measurements of new particle concentrations,
778 source rates, and spatial scales during coastal nucleation events using condensation particle counters, J.
779 Geophys. Res.-Atmos., 107, 11, 10.1029/2001jd000411, 2002.
780 Hartz, K. E. H., Tischuk, J. E., Chan, M. N., Chan, C. K., Donahue, N. M., and Pandis, S. N.: Cloud
781 condensation nuclei activation of limited solubility organic aerosol, Atmospheric Environment, 40, 605-
782 617, 10.1016/j.atmosenv.2005.09.076, 2006.
783 Heim, M., Kasper, G., Reischl, G., and Gerhart, C.: Performance of a New Commercial Electrical
784 Mobility Spectrometer, Aerosol Sci. Technol., 38, 3-14, 10.1080/02786820490519252, 2004.
785 Hermann, M., Wehner, B., Bischof, O., Han, H. S., Krinke, T., Liu, W., Zerrath, A., and Wiedensohler,
786 A.: Particle counting efficiencies of new TSI condensation particle counters, J. Aerosol. Sci., 38, 674-
787 682, 10.1016/j.jaerosci.2007.05.001, 2007.
788 Hoppel, W. A., and Frick, G. M.: The nonequilibrium character of the aerosol charge distributions
789 produced by neutralizers, Aerosol Sci. Technol., 12, 471-496, 10.1080/02786829008959363, 1990.
790 Hudson, J. G.: An Instantaneous CCN Spectrometer, J. Atmos. Ocean. Technol., 6, 1055-1065,
791 10.1175/1520-0426(1989)006<1055:aics>2.0.co;2, 1989.
792 Hudson, J. G., and Xie, Y. H.: Cloud condensation nuclei measurements in the high troposphere and in
793 jet aircraft exhaust, Geophys. Res. Lett., 25, 1395-1398, 10.1029/97gl03705, 1998.
794 IPCC, 2013: Summary for Policymakers, Intergovernmental Panel on Climate Change, Cambridge
795 University Press, 14, 2013.
796 Jennings, S. G., Geever, M., and Oconnor, T. C.: Surface CCN measurements at Mace Head, on the west
797 coast of Ireland, Nucleation and Atmospheric Aerosols 1996, 800-803, 10.1016/b978-008042030-
798 1/50193-1, 1996.
799 Jokinen, V., and Makela, J. M.: Closed-loop arrangement with critical orifice for DMA sheath excess
800 flow system, J. Aerosol. Sci., 28, 643-648, 10.1016/s0021-8502(96)00457-0, 1997.
801 Karydis, V. A., Capps, S. L., Russell, A. G., and Nenes, A.: Adjoint sensitivity of global cloud droplet
802 number to aerosol and dynamical parameters, Atmos. Chem. Phys., 12, 9041-9055, 10.5194/acp-12-
803 9041-2012, 2012.
804 Kawecki, S., and Steiner, A. L.: The Influence of Aerosol Hygroscopicity on Precipitation Intensity
805 During a Mesoscale Convective Event, J. Geophys. Res.-Atmos., 123, 424-442, 10.1002/2017jd026535,
806 2018.

Keefe, D., Nolan, P. J., and Rich, T. A.: Charge Equilibrium in Aerosols According to the Boltzmann Law, Proceedings of the Royal Irish Academy. Section A: Mathematical and Physical Sciences, 60, 27-45, 1959.
Khlystov, A.: Effect of Aerosol Volatility on the Sizing Accuracy of Differential Mobility Analyzers, Aerosol Sci. Technol., 48, 604-619, 10.1080/02786826.2014.899681, 2014.
Knutson, E. O., and Whitby, K. T.: Aerosol classification by electric mobility: apparatus, theory, and applications, J. Aerosol. Sci., 6, 443-451, https://doi.org/10.1016/0021-8502(75)90060-9, 1975.
Koehler, K. A., Kreidenweis, S. M., DeMott, P. J., Prenni, A. J., Carrico, C. M., Ervens, B., and Feingold, G.: Water activity and activation diameters from hygroscopicity data - Part II: Application to organic species, Atmos. Chem. Phys., 6, 795-809, 10.5194/acp-6-795-2006, 2006.
Kreidenweis, S. M., Koehler, K., DeMott, P. J., Prenni, A. J., Carrico, C., and Ervens, B.: Water activity and activation diameters from hygroscopicity data - Part I: Theory and application to inorganic salts, Atmos. Chem. Phys., 5, 1357-1370, 10.5194/acp-5-1357-2005, 2005.
Kumar, P. P., Broekhuizen, K., and Abbatt, J. P. D.: Organic acids as cloud condensation nuclei: Laboratory studies of highly soluble and insoluble species, Atmos. Chem. Phys., 3, 509-520, 2003.
Lance, S., Medina, J., Smith, J. N., and Nenes, A.: Mapping the operation of the DMT Continuous Flow CCN counter, Aerosol Sci. Technol., 40, 242-254, 10.1080/02786820500543290, 2006.
Leng, C. P., Cheng, T. T., Chen, J. M., Zhang, R. J., Tao, J., Huang, G. H., Zha, S. P., Zhang, M. G., Fang, W., Li, X., and Li, L.: Measurements of surface cloud condensation nuclei and aerosol activity in downtown Shanghai, Atmospheric Environment, 69, 354-361, 10.1016/j.atmosenv.2012.12.021, 2013.
Liu, X. H., and Wang, J. A.: How important is organic aerosol hygroscopicity to aerosol indirect forcing?, Environ. Res. Lett., 5, 10, 10.1088/1748-9326/5/4/044010, 2010.
Mamakos, A., Ntziachristos, L., and Sarnaras, Z.: Diffusion broadening of DMA transfer functions. Numerical validation of Stolzenburg model, J. Aerosol. Sci., 38, 747-763, 10.1016/j.jaerosci.2007.05.004, 2007.
Maricq, M. M.: Bipolar diffusion charging of soot aggregates, Aerosol Sci. Technol., 42, 247-254, 10.1080/02786820801958775, 2008.
Mei, F., Fu, H. J., and Chen, D. R.: A cost-effective differential mobility analyzer (cDMA) for multiple DMA column applications, J. Aerosol. Sci., 42, 462-473, 10.1016/j.jaerosci.2011.04.001, 2011.
Mochida, M., Kuwata, M., Miyakawa, T., Takegawa, N., Kawamura, K., and Kondo, Y.: Relationship between hygroscopicity and cloud condensation nuclei activity for urban aerosols in Tokyo, J. Geophys. Res.-Atmos., 111, 20, 10.1029/2005jd006980, 2006.
Modini, R. L., Frossard, A. A., Ahlm, L., Russell, L. M., Corrigan, C. E., Roberts, G. C., Hawkins, L. N., Schroder, J. C., Bertram, A. K., Zhao, R., Lee, A. K. Y., Abbatt, J. P. D., Lin, J., Nenes, A., Wang, Z., Wonaschutz, A., Sorooshian, A., Noone, K. J., Jonsson, H., Seinfeld, J. H., Toom-Sauntry, D., Macdonald, A. M., and Leaitch, W. R.: Primary marine aerosol-cloud interactions off the coast of California, J. Geophys. Res.-Atmos., 120, 4282-4303, 10.1002/2014jd022963, 2015.
Moore, R. H., Nenes, A., and Medina, J.: Scanning Mobility CCN Analysis-A Method for Fast Measurements of Size-Resolved CCN Distributions and Activation Kinetics, Aerosol Sci. Technol., 44, 861-871, 10.1080/02786826.2010.498715, 2010.
Moore, R. H., Bahreini, R., Brock, C. A., Froyd, K. D., Cozic, J., Holloway, J. S., Middlebrook, A. M., Murphy, D. M., and Nenes, A.: Hygroscopicity and composition of Alaskan Arctic CCN during April 2008, Atmos. Chem. Phys., 11, 11807-11825, 10.5194/acp-11-11807-2011, 2011.
Moore, R. H., Cerully, K., Bahreini, R., Brock, C. A., Middlebrook, A. M., and Nenes, A.: Hygroscopicity and composition of California CCN during summer 2010, J. Geophys. Res.-Atmos., 117, 14, 10.1029/2011jd017352, 2012.

Moore, R. H., Raatikainen, T., Langridge, J. M., Bahreini, R., Brock, C. A., Holloway, J. S., Lack, D. A., Middlebrook, A. M., Perring, A. E., Schwarz, J. P., Spackman, J. R., and Nenes, A.: CCN Spectra, Hygroscopicity, and Droplet Activation Kinetics of Secondary Organic Aerosol Resulting from the 2010 Deepwater Horizon Oil Spill, Environ. Sci. Technol., 46, 3093-3100, 10.1021/es203362w, 2012.
Ovadnevaite, J., Ceburnis, D., Martucci, G., Bialek, J., Monahan, C., Rinaldi, M., Facchini, M. C., Berresheim, H., Worsnop, D. R., and O'Dowd, C.: Primary marine organic aerosol: A dichotomy of low hygroscopicity and high CCN activity, Geophys. Res. Lett., 38, 5, 10.1029/2011gl048869, 2011.
Petters, M. D., and Kreidenweis, S. M.: A single parameter representation of hygroscopic growth and cloud condensation nucleus activity, Atmos. Chem. Phys., 7, 1961-1971, 10.5194/acp-7-1961-2007, 2007.
Petters, M. D., Prenni, A. J., Kreidenweis, S. M., and DeMott, P. J.: On measuring the critical diameter of cloud condensation nuclei using mobility selected aerosol, Aerosol Sci. Technol., 41, 907-913, 10.1080/02786820701557214, 2007.
Petters, M. D., and Kreidenweis, S. M.: A single parameter representation of hygroscopic growth and cloud condensation nucleus activity - Part 3: Including surfactant partitioning, Atmos. Chem. Phys., 13, 1081-1091, 10.5194/acp-13-1081-2013, 2013.
Rogers, R. R., and Yau, M. K.: in: A Short Course In Cloud Physics, Third ed., edited by: Haar, D. T., Elsevier Science Inc., Tarrytown, New York, USA, 87-89, 1989.
Rose, D., Gunthe, S. S., Mikhailov, E., Frank, G. P., Dusek, U., Andreae, M. O., and Poschl, U.: Calibration and measurement uncertainties of a continuous-flow cloud condensation nuclei counter (DMT-CCNC): CCN activation of ammonium sulfate and sodium chloride aerosol particles in theory and experiment, Atmos. Chem. Phys., 8, 1153-1179, 10.5194/acp-8-1153-2008, 2008.
Scanning Mobility Particle Sizer Series 5.400 and 5.500, Grimm Aerosol Technik, Ainring, Germany, 2009.
Schmale, J., Henning, S., Decesari, S., Henzing, B., Keskinen, H., Sellegri, K., Ovadnevaite, J., Pohlker, M. L., Brito, J., Bougiatioti, A., Kristensson, A., Kalivitis, N., Stavroulas, I., Carbone, S., Jefferson, A., Park, M., Schlag, P., Iwamoto, Y., Aalto, P., Aijala, M., Bukowiecki, N., Ehn, M., Frank, G., Frohlich, R., Frumau, A., Herrmann, E., Herrmann, H., Holzinger, R., Kos, G., Kulmala, M., Mihalopoulos, N., Nenes, A., O'Dowd, C., Petaja, T., Picard, D., Pohlker, C., Poschl, U., Poulain, L., Prevot, A. S. H., Swietlicki, E., Andreae, M. O., Artaxo, P., Wiedensohler, A., Ogren, J., Matsuki, A., Yum, S. S., Stratmann, F., Baltensperger, U., and Gysel, M.: Long-term cloud condensation nuclei number concentration, particle number size distribution and chemical composition measurements at regionally representative observatories, Atmos. Chem. Phys., 18, 2853-2881, 10.5194/acp-18-2853-2018, 2018.
Sem, G. J.: Design and performance characteristics of three continuous-flow condensation particle counters: a summary, Atmos. Res., 62, 267-294, 10.1016/s0169-8095(02)00014-5, 2002.
Seol, K. S., Tsutatani, Y., Camata, R. P., Yabumoto, J., Isomura, S., Okada, Y., Okuyama, K., and Takeuchi, K.: A differential mobility analyzer and a Faraday cup electrometer for operation at 200-930 Pa pressure, J. Aerosol. Sci., 31, 1389-1395, 10.1016/s0021-8502(00)00037-9, 2000.
Sinnarwalla, A. M. a. A., D.J.: A Cloud Nucleus Counter with Long Available Growth Time, Journal of Applied Meteorology, 831-835, 1973.
Stratmann, F., Kauffeldt, T., Hummes, D., and Fissan, H.: Differential electrical mobility analysis: A theoretical study, Aerosol Sci. Technol., 26, 368-383, 10.1080/02786829708965437, 1997.
Sullivan, R. C., Moore, M. J. K., Petters, M. D., Kreidenweis, S. M., Roberts, G. C., and Prather, K. A.: Timescale for hygroscopic conversion of calcite mineral particles through heterogeneous reaction with nitric acid, Phys. Chem. Chem. Phys., 11, 7826-7837, 10.1039/b904217b, 2009.
Svenningsson, B., Rissler, J., Swietlicki, E., Mircea, M., Bilde, M., Facchini, M. C., Decesari, S., Fuzzi, S., Zhou, J., Monster, J., and Rosenorn, T.: Hygroscopic growth and critical supersaturations for mixed

aerosol particles of inorganic and organic compounds of atmospheric relevance, Atmos. Chem. Phys., 6, 1937-1952, 10.5194/acp-6-1937-2006, 2006.
Wiedensohler, A.: An approximation of the bipolar charge distribution for particles in the sub-micron size range, J. Aerosol. Sci., 19, 387-389, 10.1016/0021-8502(88)90278-9, 1988.
Winkler, P.: The growth of atmospheric aerosol particles as a function of the relative humidity. II. An improved concept of mixed nuclei, J. Aerosol. Sci., 4, 373-387, 1973.
Zhao-Ze, D., and Liang, R.: Highly biased hygroscopicity derived from size-resolved cloud condensation nuclei activation ratios without data inversion, Atmospheric and Oceanic Science Letters, 7, 254-259, 2014.

Notation	
$\alpha_{CC}, \beta_{CC}, \gamma_{CC}$	Empirically-determined constants used to calculate Cunningham slip correction factor
Z_p	Aerosol particle electrical mobility
C_C	Cunningham slip correction factor
d_m	Electrical mobility diameter
n	Number of charges on particle
e	Elementary unit of charge
η	Gas dynamic viscosity
λ	Mean free path
Q_{sh}	Sheath flow
Q_e	Excess air flow
Q_a	Aerosol flow
Q_s	Sample flow
κ_{app}	Apparent hygroscopicity parameter
$\kappa_{app,artifact}$	Apparent hygroscopicity parameter artifact
s	Equilibrium water vapor saturation
s_{crit}	Critical saturation (50 % of aerosols active as cloud condensation nuclei)
A	Constant used in calculating κ_{app}
σ_{lv}	Surface tension of water
T	Temperature
D_{act}	Activation diameter
SS_{crit}	Critical percent supersaturation
α_{TF}	Height of DMA transfer function
β_{TF}	Half-width of DMA transfer function
Z_p'	Mobility of particle at DMA inlet
$Z_{p,mid}$	Midpoint of transfer function
ΔZ_p	Half-width of transfer function
V_0	Voltage selected at DMA
r_1	DMA inner radius
r_2	DMA outer radius
L	DMA length
d_{50}	50 %-cut-off diameter

912

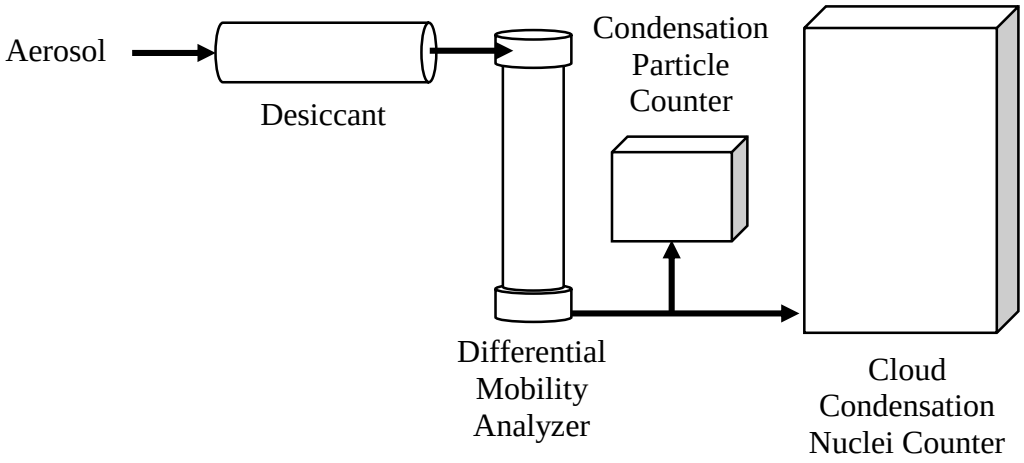

Figure 1 Experimental setup used for obtaining sized CCN and particle concentration measurements from an aerosol sample.

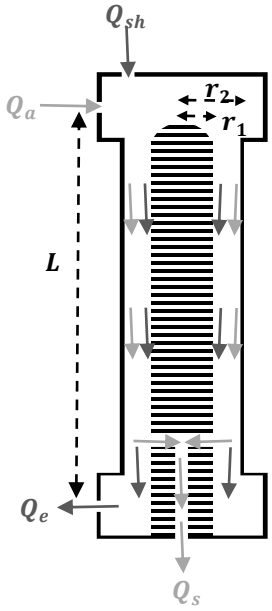

916

917 **Figure 2** Simplified flow diagram of a DMA with an inner electrode radius r_1, outer electrode radius r_2,

918 distance between aerosol inlet and sample outlet L, clean sheath air flow Q_{sh}, aerosol flow Q_a, excess air

919 flow Q_e, and sample air flow Q_s.

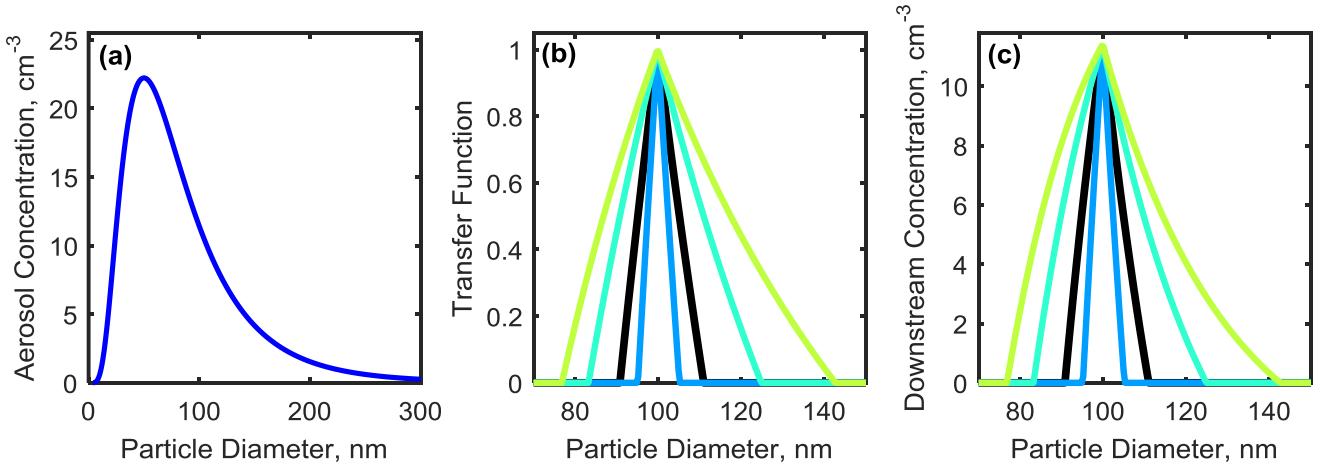

920

921

922 **Figure 3** (a) A theoretical aerosol distribution generated using a lognormal function centered at 50 nm. .

923 (b) The transfer function calculated using Eq. (7). (c) Multiplying the distribution by the transfer function

924 gives the downstream aerosol concentration (cm^{-3}).

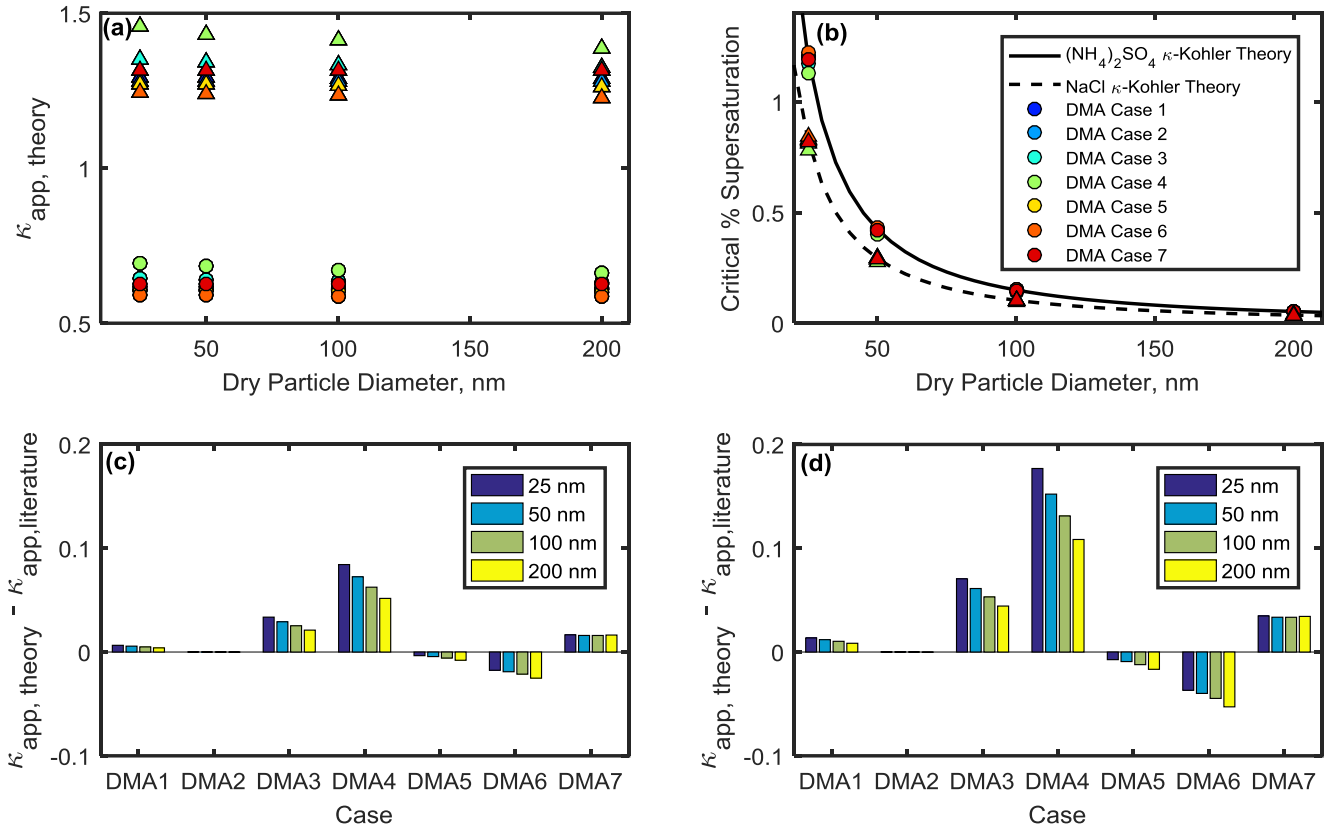

925

926 **Figure 4** (a) Apparent hygroscopicity κ_{app} for DMA cases 1-7 for sodium chloride (triangles) and

927 ammonium sulfate (circles) [see legend in (b)]. (b) Critical supersaturation of ammonium sulfate and

928 sodium chloride particles calculated using κ_{app} values derived in (a). Ammonium sulfate and sodium

929 chloride curves from κ-Köhler theory are shown for comparison. Legend colors apply to both salts.

930 (c,d) DMA-flow-derived artifacts in κ_{app} are shown for each DMA case and both salts.

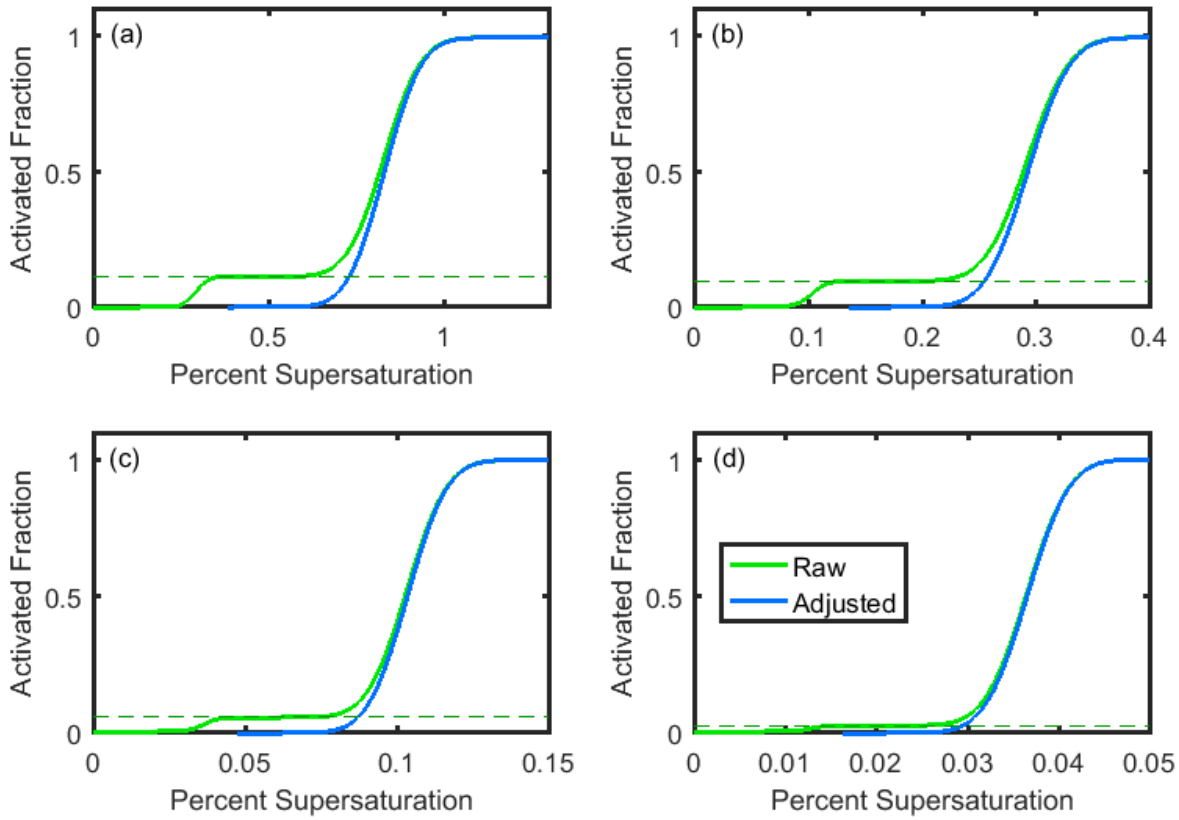

931

932 **Figure 5** Theoretical raw (green) and adjusted (blue) activated fraction curves for (a) 25 nm (+1), 50 nm

933 (+2), and 75 nm (+3) particles; (b) 50 nm (+1), 100 nm (+2), and 150 nm (+3) particles; (c) 100 nm

934 (+1), 200 nm (+2), and 300 nm (+3) particles; (d) 200 nm (+1), 400 nm (+2), and 600 nm (+3) particles.

935 All particles are pure sodium chloride.

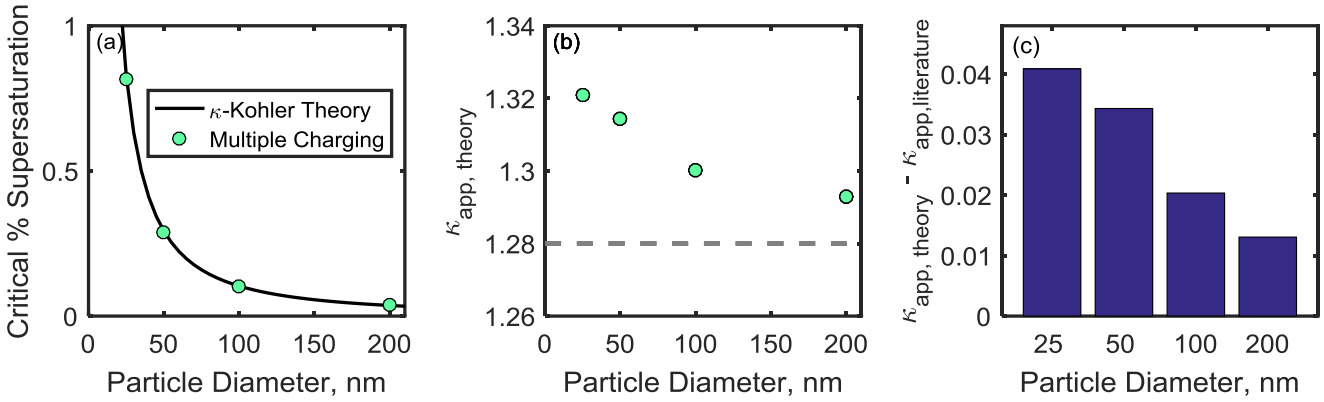

936

937 **Figure 6** (a) Critical percent supersaturation of sodium chloride particles determined from activated

938 fraction curves shown in Fig. 5. A κ-Köhler curve for sodium chloride is shown for comparison. (b)

939 Theoretical κ_{app} for each particle diameter (gray dashed line indicates literature value for κ_{app}^{NaCl}). (c)

940 Artifacts in κ_{app} resulting from multiple particle charges.

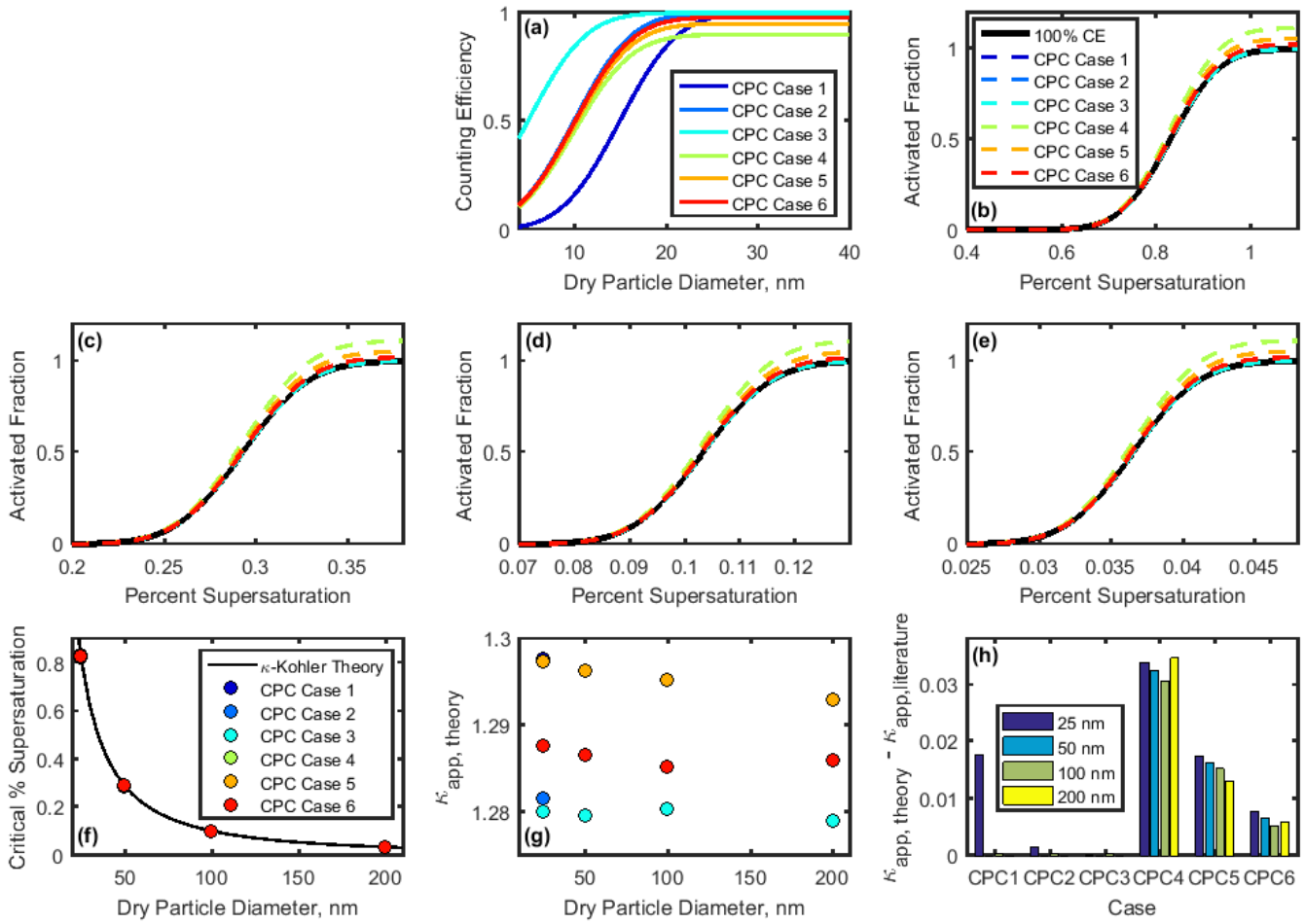

941

942 **Figure 7** (a) Counting efficiency curves for CPC Cases 1-6 (shown in Table 3).

943 (b-e) CCN activated fraction curves for 25, 50, 100, and 200 nm NaCl, respectively. (f) Critical

944 supersaturation calculated for each particle diameter. (g) Theoretical κ_{app} for each CPC case and

945 particle diameter. (h) Artifacts in κ_{app} for each CPC case and particle diameter.

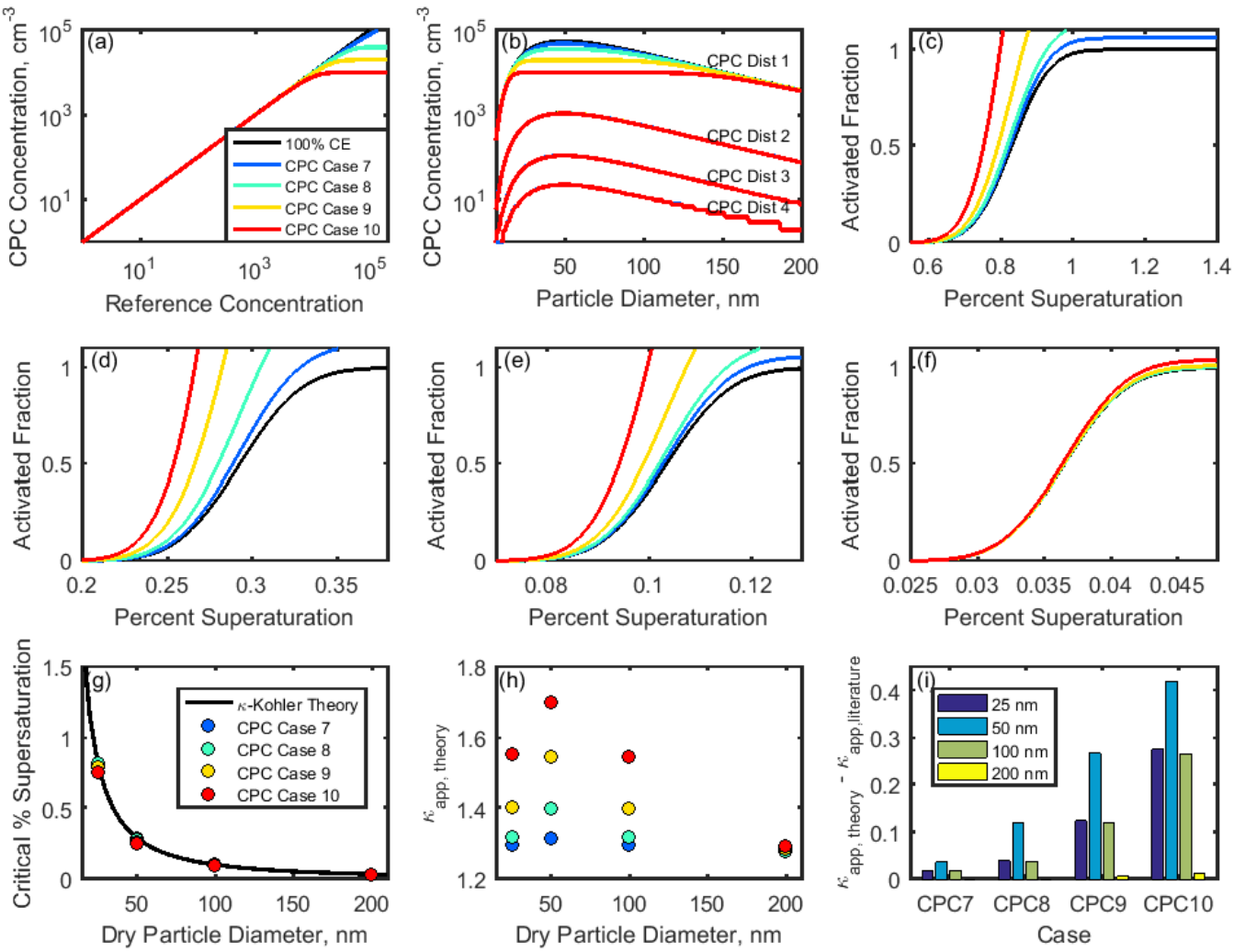

946

947 **Figure 8** (a) Theoretical relationships between the reference aerosol concentration and CPC

948 concentration. (b) Concentration-dependent counting efficiencies from (a) were applied to four

949 theoretical aerosol distributions. (c-f) Activated fraction curves for CPC Distribution 1 and particle

950 diameters 25, 50, 100, and 200 nm NaCl aerosol, respectively. (g,h) Critical supersaturation and κ_{app} for

951 each case. (i) Artifacts in κ_{app} for each case.

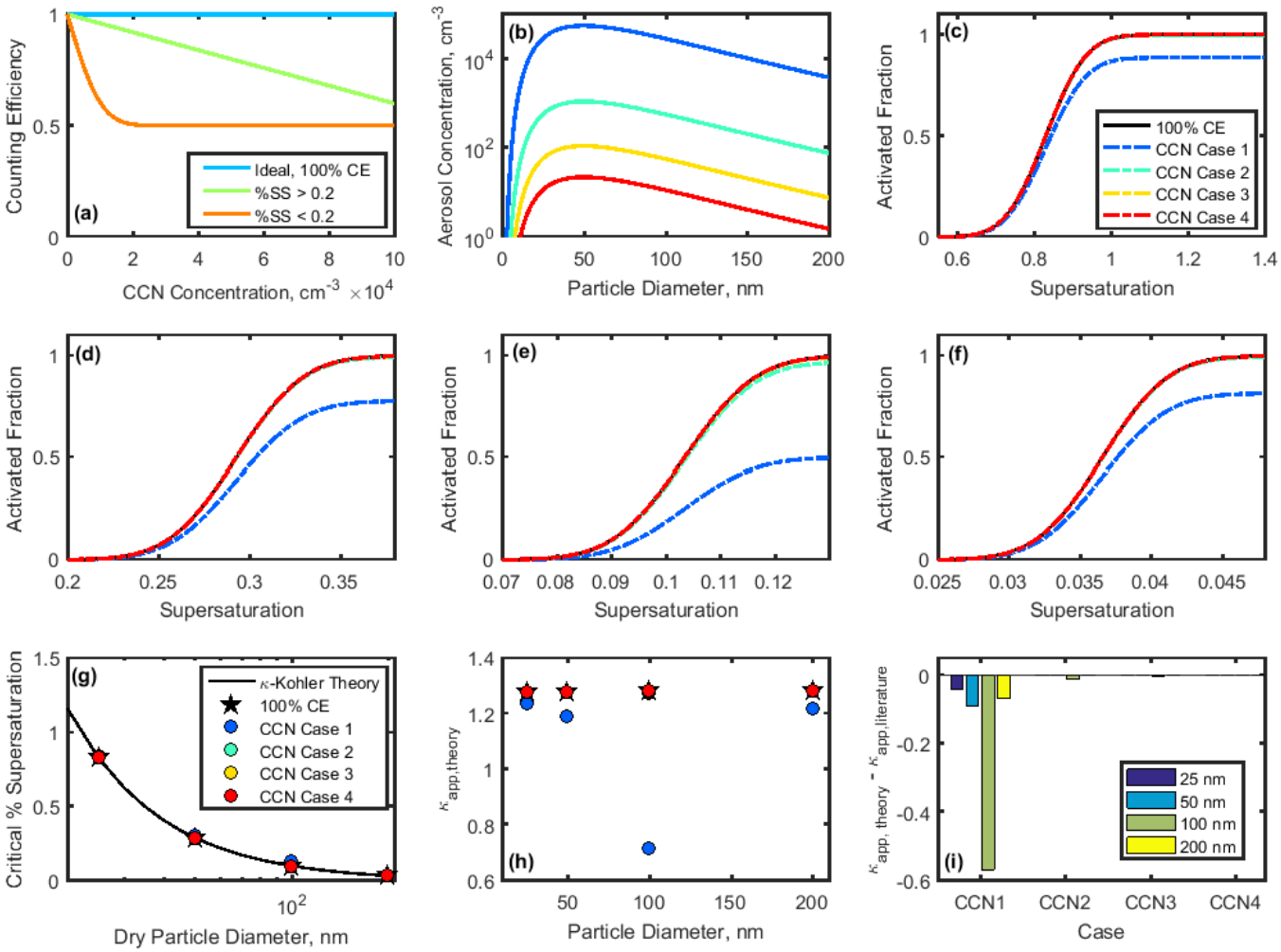

Figure 9 (a) Counting efficiencies of the DMT CCN-100 for specific supersaturations. (b) Lognormal aerosol distributions used to study CCN undercounting at high concentrations. (c-f) Activated fraction curves for 25, 50, 100, and 200 nm NaCl particles. Supersaturation-specific counting efficiencies from (a) applied to theoretical sigmoid curves for NaCl CCN activation. Activated fraction in the case of 100 % counting efficiency is shown for comparison. (g) Critical supersaturation for each case. (h) Theoretical κ_{app} calculated for each case. (i) Artifacts in κ_{app} artifacts for each case.

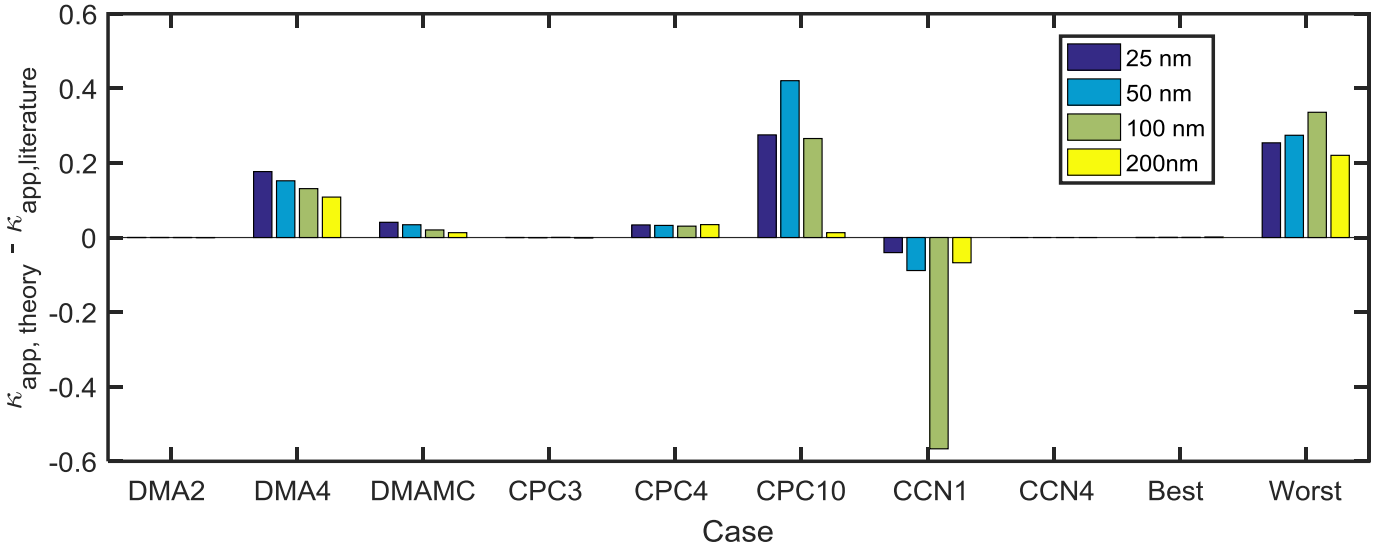

959

960 **Figure 10** Comparison of κ_{app} artifacts derived from best and worst case scenarios for instrumental

961 measurements for sodium chloride. Combined artifacts for the lowest-artifact cases (Best: DMA Case

962 2, CPC Case 3, and CCN Case 4) and the highest-artifact cases (Worst: DMA Case 4, multiple charging,

963 CPC Case 4, CPC Case 8, and CCN Case 1).

964

Table 1 Theoretical DMA Flow Test Cases

Case	Q_{sh} (L min^{-1})	Q_e (L min^{-1})	Q_a (L min^{-1})	Q_s (L min^{-1})	Q_a/Q_{sh}	Q_e/Q_{sh}
DMA 1	3.00	3.00	0.30	0.30	0.10	1.00
DMA 2	3.00	3.00	0.15	0.15	0.05	1.00
DMA 3	3.00	3.00	0.60	0.60	0.20	1.00
DMA 4	3.00	3.00	0.90	0.90	0.30	1.00
DMA 5	3.00	3.06	0.36	0.30	0.12	1.02
DMA 6	3.00	3.15	0.45	0.30	0.15	1.05
DMA 7	3.00	2.94	0.24	0.30	0.08	0.98

Table 2 Predicted downstream particle diameter range for each DMA case.				
Case	25 nm	50 nm	100 nm	200 nm
DMA 1	23-27	46-56	91-111	181-222
DMA 2	24-26	48-53	95-105	190-211
DMA 3	21-31	42-62	83-125	167-250
DMA 4	20-36	39-71	77-143	154-285
DMA 5	23-27	45-55	90-110	181-220
DMA 6	22-27	45-54	89-107	178-215
DMA 7	23-28	46-56	92-112	183-225

966

Table 3 Values of 50%-cutoff diameter and maximum counting efficiency used in investigating κ_{app} artifacts for low particle concentrations measured by a CPC.

Case	d_{50}, nm	Maximum Counting Efficiency
CPC 1	15	100 %
CPC 2	10	100 %
CPC 3	5	100 %
CPC 4	10	90 %
CPC 5	10	95 %
CPC 6	10	98 %

967

Table 4 Equations used to model the relationship between a reference or "true" aerosol concentration x (particles cm^{-3}), and the concentration measured by a condensation particle counter y (particles cm^{-3}).

Case	Equation
CPC 7	$y = x - 2 \times 10^{-6} x^2$
CPC 8	$y = 40000 \operatorname{erf}\left(\frac{x}{32000\sqrt{2}}\right)$
CPC 9	$y = 20000 \operatorname{erf}\left(\frac{x}{16000\sqrt{2}}\right)$
CPC 10	$y = 10000 \operatorname{erf}\left(\frac{x}{8000\sqrt{2}}\right)$

968

Table 5 Total concentrations used in theoretical aerosol distribution for CPC operation at high concentration and CCN-derived κ_{app} artifacts.

CPC Distribution	CCN Case	Total Concentration (particles cm^{-3})
CPC Distribution 1	CCN 1	5×10^6
CPC Distribution 2	CCN 2	1×10^5
CPC Distribution 3	CCN 3	1×10^4
CPC Distribution 4	CCN 4	2×10^3

969